PHYSICAL REVIEW FLUIDS **6**, 044306 (2021)

Featured in Physics

Sedimentation of inertial monodisperse suspensions of cubes and spheres

Arman Seyed-Ahmadi[1] and Anthony Wachs[1,2,*]
[1]*Department of Chemical and Biological Engineering, University of British Columbia,*
2360 East Mall, Vancouver, BC, V6T 1Z3, Canada
[2]*Department of Mathematics, University of British Columbia, 1984 Mathematics Road,*
Vancouver, BC, V6T 1Z2, Canada

(Received 24 October 2020; accepted 9 March 2021; published 21 April 2021)

Particle-resolved direct numerical simulations of monodisperse settling suspensions of cubes and spheres are performed for Galileo numbers $\mathrm{Ga} = 70$ and $\mathrm{Ga} = 160$, and solid volume fractions in the range $0.01 \leqslant \phi \leqslant 0.2$. The solid-to-fluid density ratio $m = \rho_s/\rho_f$ is taken to be fixed at 2, representing liquid-solid suspensions. Strong columnar clustering is observed for $\mathrm{Ga} = 160$ and $\phi = 0.01$ in a sphere suspension, whereas similar vertical structures are not present as prominently in a cube suspension. We find that in all cases, cube suspensions tend to be more homogeneous compared to sphere suspensions, as indicated by both their microstructure and momentum transfer properties. The enhanced homogeneity is associated with the pronounced angular velocities of cubes and the resulting orientation- and rotation-induced lift forces, which promote transverse motions and the likelihood of escaping from clusters. Higher rotation rates of cubes thus play a major role in the transfer of momentum from the gravity to the transverse direction, demonstrated by the lower anisotropy of particle velocity fluctuations in cube suspensions. In more dilute cases, cubes induce significantly stronger pseudoturbulence in the flow, especially in the transverse direction. The drag of dynamic cube suspensions is found to be generally similar to static beds of cubes, the reason for which is speculated to be relevant to their motion freedom and the more homogeneous microstructure.

DOI: 10.1103/PhysRevFluids.6.044306

I. INTRODUCTION

The gravity-driven motion of sedimenting particles is one of the most commonly occurring phenomena in numerous natural and industrial processes. Rain formation and precipitation, sediment transport in rivers, and particle settling in fluidized beds and waste-water treatment tanks are examples of situations where collective sedimentation of suspended particles plays a central role. Settling suspensions are complex systems that are rife with rich dynamics stemming from various factors. While a large number of governing parameters are typically involved (e.g., mass and volume loading, flow regime, particle shape and rigidity, configuration), there is also a wide range of spatial and temporal scales associated with the occurring physical phenomena. In liquid-solid suspensions, which are the focus of this study, the timescale of particle collisions is generally an order of magnitude smaller than that of the flow evolution. Moreover, flow disturbances on the scale of particle dimensions are known to influence overall hydrodynamics of suspensions and collective behavior of particles. For example, clusters that form as a result of wake interactions may span several particle diameters and persist over relatively long periods of time [1,2].

---

[*] Corresponding author: wachs@math.ubc.ca

The most idealized picture of particle settling has emerged from the pioneering work of Stokes [3], giving the drag force acting on a single rigid sphere settling in an unbounded quiescent fluid to be $3\pi \mu D V_{z,s}$, where μ and D are the dynamic viscosity of the fluid and the particle diameter, respectively, whereas $V_{z,s}$ denotes the particle settling velocity. This relation is valid under the assumption of vanishing inertia or $\mathrm{Re} \to 0$, with Re being the Reynolds number defined as $\mathrm{Re} = \rho_f V_{z,s} D/\mu$ and ρ_f the density of the fluid. For a particle cluster in an infinite domain, the settling velocity would always be greater than that of a single settling particle as a result of hydrodynamic cooperation between the particles [4]. When particles settle in a container with a fixed bottom wall, however, the motion is hindered since the downward flux of the solid particles and the adjoining fluid needs to be compensated for by an upward fluid flux (also called "back-flow"), thus making the mixture average velocity vanish over the entire suspension. A general theoretical treatment of settling suspensions has been beyond reach due to the complexity of Navier-Stokes equations given the presence of nonlinear inertial terms. Even if inertia is ignored (i.e., Stokes flow) and the governing equations consequently become linear, superposition of velocity disturbances of individual spheres leads to a diverging integral due to the slow decay of perturbations in Stokes flow. Using probability arguments, Batchelor [5] circumvented the divergence problem and showed that the hindered settling velocity of a dilute suspension of rigid spheres for $\mathrm{Re} \ll 1$ is given by

$$\frac{V_z}{V_{z,s}} = 1 - 6.55\phi, \tag{1}$$

where V_z denotes the ensemble average of the suspension settling velocity, $V_{z,s}$ the terminal settling velocity of an isolated sphere and ϕ the solid volume fraction. For higher solid volume fractions and Reynolds numbers, empiricism is inevitable for obtaining the settling velocity as a function of the solid volume fraction. The most widely known formula is the power-law relation of Richardson and Zaki [6] given as

$$\frac{V_z}{V_{z,s}} = (1 - \phi)^n, \tag{2}$$

which was obtained from experimental data of sedimentation and fluidization of dense suspensions (i.e., $\phi \geqslant 0.1$), and is believed to be accurate for $\mathrm{Re} \leqslant 25$ [7] and concentrations up to $\phi = 0.25$ [8]. Based on extensive experimental data [6], values of the exponent n were shown to depend on the flow regime, having a constant value for both very low (Stokes regime) and very high (Newton regime) Reynolds numbers, and a transition region for intermediate values of Re. A compact form of the dependence of n on Re was given by Garside and Al-Dibouni [9] as the logistic curve

$$\frac{5.1 - n}{n - 2.7} = 0.1\mathrm{Re}^{0.9}, \tag{3}$$

which improves the accuracy of Eq. (2) for higher Reynolds numbers. Later Di Felice [10] showed through settling experiments that the exponent n in dilute suspensions with $\phi \leqslant 0.05$ is approximately 1.5 times larger than that for denser suspensions, although having a similar functional dependence on Re. Di Felice [10] also noted that with n being higher for dilute suspensions, the hindrance function in Eq. (2) needs a correction prefactor k for concentrated suspensions, values of which were suggested to be between 0.8 and 0.9. The rapid decay of the settling velocity for $\mathrm{Re} > 1$ especially at low concentrations was later confirmed by Yin and Koch [11] and Hamid *et al.* [12] through numerical simulations. The departure from the power-law relation of Eq. (2) was observed to be more pronounced for higher Re. Consequently, this was attributed to the formation of inhomogeneous structures in the suspensions as a result of enhanced wake interaction between spheres in more inertial flows [11,12], hinting that a power-law form for the hindrance function is possibly associated with a hard-sphere (i.e., random) distribution of the particles.

In Stokes regime, the flow field produced around a settling sphere has fore-aft symmetry [13]. Additionally, two nearby settling particles will maintain their relative orientation and separation, and will always fall faster than an isolated particle according to symmetry and reversibility properties of

Stokes flow [4]. As the flow becomes inertial upon increasing the Reynolds number, the symmetry is lost and a low-pressure wake region develops downstream of the sphere. A particle that happens to be in the wake of another experiences less drag compared to an isolated one, which consequently causes it to accelerate (“drafting” phase) towards the leading particle. The trailing particle is also subject to a lift force due to the shear flow in the wake region and is hence pushed outwards at the same time [14]. If the induced lift force is not sufficiently strong, the trailing particle touches (“kissing” phase) the leading one. Since the vertical arrangement of the pair is unstable, the particles rotates into a horizontal orientation (“tumbling” phase) and then they repel each other due to the source flow pushing the fluid away from the particles. This robust sequence of Drafting, Kissing, and Tumbling (DKT) [15] has been identified in several investigations in the past [1,2,11,12,16–20] as the principal mechanism underlying the emergence and evolution of anisotropic, inhomogeneous particle configurations in sedimenting suspensions. The aforementioned deviation of the settling velocity from Eq. (2) in inertial suspensions is in fact explained by the frequent occurrence of the DKT phenomenon [11,12]. Wake attraction and the ensuing horizontal arrangements, also known as “rafts” [21], effectively reduce the likelihood of particles being in the wake of others. Horizontally arranged particles in cross-stream configuration experience higher drag [22] and reduced settling velocity as a result. The prevalence of horizontal structure of particle clusters has been reported by Yin and Koch [11] at low Reynolds numbers and recently observed by Willen and Prosperetti [16] in moderately dense suspensions with $\phi = 0.087$ and Reynolds numbers as high as $\mathrm{Re} \simeq 111$.

The forgoing scenario of settling rate reduction resulting from DKT-induced dispersion has turned out to be entirely different for dilute suspensions when the Reynolds number is increased to $\mathrm{Re} = O(100)$. On the one hand, the combination of stronger wakes in higher Re and low particle concentration allows particles to interact over longer distances without being interrupted by other particles. On the other hand, the occurrence of wake instabilities and resulting lateral motions in highly inertial regimes increases the probability of particles crossing paths. The wake of an isolated sphere first undergoes a transition from an axisymmetric to a double-threaded plane-symmetric wake at $\mathrm{Re} \simeq 210$ [23,24], inducing a steady side force. The subsequent transition at $\mathrm{Re} \simeq 275$ initiates periodic vortex shedding and oscillating transverse forces. These wake instabilities give rise to a variety of different path geometries for a freely settling particle. In the case of a freely moving particle, the regimes of motion are characterized by two dimensionless numbers: namely, the density ratio $m = \rho_s/\rho_f$, and the Galileo number $\mathrm{Ga} = \sqrt{(m-1)gD^3}/\nu$, with ρ_s showing the solid density, g the gravitational acceleration, and ν the kinematic viscosity of the fluid. As a result of wake transitions, a vertically settling sphere switches to a steady oblique path for $\mathrm{Re} \geqslant 210$ [25] or equivalently for $\mathrm{Ga} \geqslant 150$ [26], while various patterns of oblique-oscillating paths for $185 \leqslant \mathrm{Ga} \leqslant 215$ emerge depending on the density ratio m [27]. Chaotic paths are usually observed for settling spheres beyond $\mathrm{Ga} \simeq 250$ [26–28]. The collective behavior of particles in such highly inertial regimes was first investigated numerically by Kajishima and Takiguchi [20]. Through their particle-resolved direct numerical simulations (PR-DNS) of dilute (i.e., $\phi = 0.002$) sphere suspensions, they evidenced strong particle accumulation and increased settling velocities for $\mathrm{Re} \geqslant 300$, for which wake attraction was identified as the responsible mechanism. More recently, PR-DNS of Uhlmann and Doychev [1] showed that in dilute suspensions ($\phi = 0.005$), settling velocity is enhanced by up to 12% at $\mathrm{Ga} = 178$, while no significant changes were seen for a similar suspension at $\mathrm{Ga} = 121$. This was explained by the fact that at $\mathrm{Ga} = 178$, spheres settle in oblique paths, increasing the probability of getting trapped in the wake of another sphere and consequently undergoing DKT-type interactions. Frequent DKT between spheres results in the formation of sizable clusters which settle considerably faster than an isolated sphere, or compared to the other simulated case at a lower Galileo number of $\mathrm{Ga} = 121$. This enhancement of settling rate is clearly in stark contrast with the aforementioned reduction of settling rate in dilute suspensions with $\mathrm{Re} = O(10)$. Similar wake-induced clustering and increased settling rates for highly inertial dilute suspensions were also consistently reported by Zaidi *et al.* [2] and experimentally confirmed later by Huisman *et al.* [18]. Interestingly, the authors of the latter study reported less enhanced settling velocities for $\mathrm{Ga} = 310$ compared to $\mathrm{Ga} = 170$. They suspected the observed behavior to be owing to the chaotic wakes of the particles in the $\mathrm{Ga} = 310$ case, which might increase the likelihood of particles to break free from clusters.

Another level of complexity in studying suspension flows originates from the introduction of nonspherical particles. While a general understanding of suspensions of spheres has been progressively accumulating over the past years, especially concerning low to moderate Reynolds numbers (i.e., $\mathrm{Re} \leqslant 50$), no such knowledge is currently available for suspensions of nonspherical particles. Freely moving nonspherical objects exhibit various path geometries due to both the anisotropy of added-mass tensor and wake instabilities [29]. Moreover, their nature of hydrodynamic interactions in multiparticle systems can be greatly different from spheres. The orientation of a nonspherical particle also plays an important role in its overall dynamics, not only by affecting hydrodynamic forces but also through inducing hydrodynamic torques that would otherwise be either negligible or absent [30–32]. The introduced torques promote particle rotations, which in turn, give rise to additional hydrodynamic loads such as the Magnus force [28]. While the dynamics of a free sphere is reasonably well fleshed out for various regimes [25–27,33], fewer studies have been dedicated to the characterization of motion regimes for isolated nonspherical particles in the existing body of literature. Thus far, free motion of objects such as disks [34–36], short cylinders [37], long cylinders [38,39], oblate and prolate spheroids [40], and angular objects such as cubes and tetrahedrons [28,41] have been investigated. Expectedly, the motion and flow characteristics associated with nonspherical particles bear significant implications for their corresponding settling suspensions. This is exemplified, for instance, through the recent work of Ardekani *et al.* [40] on free settling of oblate and prolate spheroids. They showed that since oblate particles have considerably wider wake regions compared to spheres, they become drawn into the wake of one another over considerably larger horizontal separations. The higher susceptibility for wake attraction was shown to be translated into the remarkable formation of columnar clusters in dilute suspensions of oblate spheroids at $\mathrm{Ga} = 60$ [7]. Consequently, the settling speed was reported to be $\simeq 30\%$ larger than that of a single oblate particle. As for other shapes, there are a limited number of studies that consider suspensions of nonspherical particles such as the settling of particles shaped like red blood cells with $\mathrm{Re} \simeq 1$ and high volume fractions [42], cylindrical particles with $1 \leqslant \mathrm{Re} \leqslant 10$ and $0.1 \leqslant \phi \leqslant 0.48$ [43], rodlike objects with $\mathrm{Re} = 0.07$ and $0.01 \leqslant \phi \leqslant 0.1$ [44], long fibers with $\mathrm{Re} \leqslant 10^{-4}$ [45], and flexible long fibers at $\mathrm{Ga} = 160$ in dilute and semidilute regimes [46]. Evidently, most of the available works on nonspherical particle suspensions are carried out for systems at low Reynolds numbers with the exception of a few.

Polyhedral solids are commonly encountered in soil, rock, and mining engineering processes as well as powder metallurgy applications. In particular, metal powders made of cubic particles can be produced by electrolysis of solid metal oxide particles in molten salts [47]. Moreover, cubic particles also find use as catalysts, absorbents, and ferro-fluids in the form of metal colloids [48]. Considering its rich dynamics [41], the cube is an interesting shape for studying effects of nonsphericity on the behavior of suspensions. The cube belongs to a class of regular polyhedrons known as Platonic solids, shown in Fig. 1, which are highly symmetrical convex shapes constructed from flat polygonal faces of the same size. Similar to the case of a sphere, only one parameter needs to be prescribed to fully define the geometry of a cube. This feature makes the exploration of the parameter space for any one of the five regular polyhedrons considerably easier compared to other nonspherical shapes, e.g., cylinders or spheroids. The existence of sharp edges and rapid variation of hydrodynamic loads upon changes in its orientation make the cube prone to strong translational and rotational displacements and velocity fluctuations. In fact, we have recently provided a comprehensive flow map of the free motion of a cube [41], complementing a previous study by our group on the motion of isolated angular particles [28]. Along with identifying a robust regime of helical motion for $140 \leqslant \mathrm{Ga} \leqslant 170$, we found that while a settling sphere is still in the oblique regime at $\mathrm{Ga} = 180$ [25,49], the cube already moves chaotically with large velocity fluctuations at the same Ga. Moreover, a cube acquires angular velocities that are at least an order of magnitude larger than that of a sphere for $\mathrm{Ga} \geqslant 160$, which induce significant Magnus forces normal to the direction of motion. Additionally,

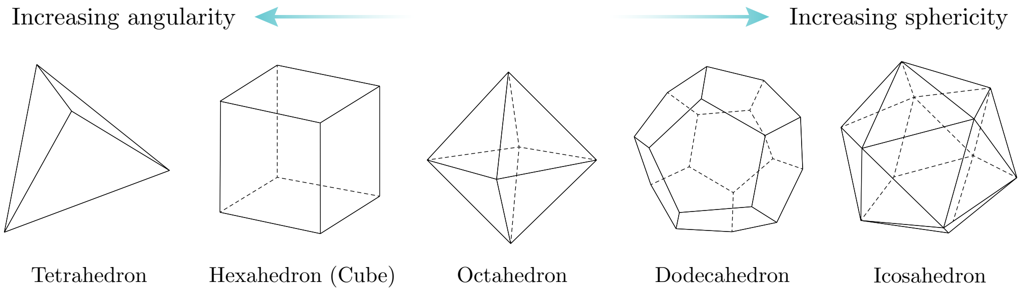

FIG. 1. The five regular convex polyhedrons, also known as Platonic solids, in the order of increasing number of faces.

the magnitude of lateral forces caused by intense vortex shedding rises to about 25% of the net buoyancy force driving the motion. Motivated by the aforementioned remarkable features, we are especially curious to find out whether the more agitated motion character of a cube could promote mixing and alter momentum transfer properties in suspensions of cubes, and the extent to which these properties might differ from that of sphere suspensions. To this end, we study suspensions of cubes for two different Galileo numbers: namely, $\mathrm{Ga} = 70$ and $\mathrm{Ga} = 160$, and solid volume fractions in the range of $0.01 \leqslant \phi \leqslant 0.2$. In order to establish grounds for comparison, we also simulate suspensions of spheres for the same set of values of Ga and ϕ. It should be stressed that there is not anything specific about the shape of a cube compared to other Platonic polyhedrons; however, given that performing simulations for all such shapes is computationally not possible at present, we have selected the cube as a representative for convex polyhedrons in general.

In what follows, first the numerical methodology implemented in our PR-DNS tool and the setup of the simulations are described in Sec. II. We then proceed to the simulation results in Sec. III, beginning with particle dynamics in Secs. III A to III C in terms of settling rates, velocity fluctuations, and angular velocities of the particles. Subsequently, detailed description of suspension microstructure is presented in Sec. III D, followed by drag force analysis in Sec. III E. Finally, we conclude the article in Sec. IV with a summary of our findings in the present work, along with a discussion of possible mechanisms for the observed differences between suspensions of cubes and spheres.

II. COMPUTATIONAL METHODOLOGY

A. Governing equations

The conservation of momentum and mass for an incompressible Newtonian fluid is described through Navier-Stokes equations, which are given as

$$\frac{\partial \mathbf{u}}{\partial t} + \mathbf{u} \cdot \boldsymbol{\nabla} \mathbf{u} = -\boldsymbol{\nabla} p + \frac{1}{\mathrm{Ga}} \nabla^2 \mathbf{u}, \tag{4}$$

$$\boldsymbol{\nabla} \cdot \mathbf{u} = 0, \tag{5}$$

where $\mathbf{u}$ and p are the fluid velocity vector and pressure, respectively. In Eq. (4) Ga may be thought of as a Reynolds number based on the gravitational velocity scale u_g, the definitions of which are

$$\mathrm{Ga} = \frac{\rho_f u_g D}{\mu}, \tag{6}$$

$$u_g = \sqrt{(m-1)gD}, \tag{7}$$

with D being the volume-equivalent diameter of a particle. Based on u_g, a gravitational timescale $t_g = D/u_g$ may also be defined. The solid-to-fluid density ratio m together with the Galileo number

Ga and solid volume fraction ϕ are the three governing parameters for the problem of gravity-driven evolution of a monodisperse suspension of particles. Furthermore, the rigid-body motion of each particle is described by the Newton-Euler equations, which in the body frame of reference may be written as

$$m v_p \frac{d\mathbf{V}}{dt} = \mathbf{F}_h + \mathbf{F}_c + (m-1) v_p \mathbf{g}, \tag{8}$$

$$m \mathbf{I}_p \frac{d\mathbf{\Omega}}{dt} + \mathbf{\Omega} \times (\mathbf{I}_p \cdot \mathbf{\Omega}) = \mathbf{T}_h + \mathbf{T}_c, \tag{9}$$

where $\mathbf{V}$, $\mathbf{\Omega}$, v_p, and $\mathbf{I}_p$ stand for the translational and angular velocity vectors, volume, and inertia tensor of the particle, respectively, whereas $\mathbf{g}$ shows the gravitational acceleration vector. Note that $\mathbf{I}_p$ is a scalar matrix for spheres and cubes, hence $\mathbf{\Omega} \times (\mathbf{I}_p \cdot \mathbf{\Omega}) = 0$. In Eq. (8) $\mathbf{F}_c$ and $\mathbf{T}_c$ show forces and torques arising from collisions between the particles, the computation of which is handled by contact mechanics approaches and will be presented in the next section. The hydrodynamic force and torque exerted on a particle are denoted by $\mathbf{F}_h$ and $\mathbf{T}_h$ and given as

$$\mathbf{F}_h = \int_S \left[-p\mathbf{I} + \frac{1}{\mathrm{Ga}} (\nabla \mathbf{u} + \nabla \mathbf{u}^T) \right] \cdot \mathbf{n} \, dS, \tag{10}$$

$$\mathbf{T}_h = \int_S \mathbf{r} \times \left[-p\mathbf{I} + \frac{1}{\mathrm{Ga}} (\nabla \mathbf{u} + \nabla \mathbf{u}^T) \right] \cdot \mathbf{n} \, dS, \tag{11}$$

with $\mathbf{I}$ being the identity matrix, $\mathbf{n}$ the unit vector normal to the boundary of the solid, S the surface enclosing the solid, $(\,\cdot\,)^T$ the matrix transpose, and $\mathbf{r}$ the position vector relative to the solid center of mass.

B. Numerical method

Our PR-DNS tool PeliGRIFF (Parallel efficient library for GRains in Fluid Flow) incorporates a finite-volume variant of the distributed Lagrange multiplier-fictitious domain (DLM-FD) formulation proposed by Glowinski *et al.* [50] for fluid-solid coupling, while the interparticle collisions are handled by an efficient Discrete Element Method (DEM) granular solver. In the framework of the DLM-FD method, the fluid domain is extended to the solid region where rigid-body motions are enforced in the fictitious fluid inside the particles through a set of collocated Lagrange multipliers. Here we present a brief description of the method, and refer the interested reader to [51–54] where the details of our implementation have been elaborated. In a nonvariational form, the combined momentum and continuity equations are given as

$$\frac{\partial \mathbf{u}}{\partial t} + \mathbf{u} \cdot \nabla \mathbf{u} = -\nabla p + \frac{1}{\mathrm{Ga}} \nabla^2 \mathbf{u} - \lambda \text{ in } \mathbb{D}, \tag{12}$$

$$(m-1) v_p \frac{d\mathbf{V}}{dt} - \int_{\mathbb{P}} \lambda d\mathbf{x} = \sum_j \mathbf{F}_{cj} + (m-1) v_p \mathbf{g} \text{ in } \mathbb{P}, \tag{13}$$

$$(m-1) \mathbf{I}_p \frac{d\mathbf{\Omega}}{dt} - \int_{\mathbb{P}} \mathbf{r} \times \lambda d\mathbf{x} = \sum_j \mathbf{r}_j \times \mathbf{F}_{cj} \text{ in } \mathbb{P}, \tag{14}$$

$$\mathbf{u} - (\mathbf{V} + \mathbf{\Omega} \times \mathbf{r}) = 0 \text{ in } \mathbb{P}, \tag{15}$$

$$\nabla \cdot \mathbf{u} = 0 \text{ in } \mathbb{D}, \tag{16}$$

where the solid domain and combined fluid/particle domain are denoted by $\mathbb{P}$ and $\mathbb{D}$, respectively. Also, λ shows the distributed Lagrange multiplier vector which is used to enforce the rigid-body motion constraint shown in Eq. (15). With the DLM-FD method, the Lagrange multiplier λ can be directly used to obtain the hydrodynamic force and torque exerted on a particle $\mathbb{P}$ as follows:

$$\mathbf{F}_h = \int_{\mathbb{P}} \lambda d\mathbf{x} + v_p \frac{d\mathbf{V}}{dt}, \tag{17}$$

$$\mathbf{T}_h = \int_{\mathbb{P}} \mathbf{r} \times \lambda d\mathbf{x} + \mathbf{I}_p \frac{d\boldsymbol{\Omega}}{dt}. \tag{18}$$

The time-marching algorithm employed for the solution of Eqs. (12) to (16) is described in the Appendix. In order to handle interparticle collisions, we consider the total contact force to be the sum of three contributions: namely, a normal Hookean elastic restoring force, a normal dissipative force, and a tangential friction force. The elastic restoring force is given as

$$\mathbf{F}_e = k_n \delta \mathbf{n}_{ij,} \tag{19}$$

where k_n represents the equivalent spring stiffness, δ the overlap between particles i and j, and $\mathbf{n}_{ij}$ the normal unit vector at the contact point. Furthermore, the viscous dissipative force is defined as

$$\mathbf{F}_{dn} = -2\gamma_n M_{ij} \mathbf{V}_n, \tag{20}$$

where γ_n denotes the normal damping coefficient, and $M_{ij} = (m_i m_j)/(m_i + m_j)$ the reduced mass of particles i and j having masses m_i and m_j, respectively. In Eq. (20) $\mathbf{V}_n$ shows the normal component of the relative velocity between particles i and j. γ_n can be related to k_n through the restitution coefficient e_n defined as the postcollisional to precollisional velocity ratio in the normal direction. In the case of a purely normal collision between two spherical particles in a zero gravity space, we can solve analytically the contact problem and establish the following relationship [52,55]:

$$\gamma_n = -\sqrt{\frac{k_n}{M_{ij}}} \frac{\ln e_n}{\sqrt{\pi^2 + (\ln e_n)^2}}. \tag{21}$$

The tangential friction force is given as

$$\mathbf{F}_t = -\min\{\mu_c |\mathbf{F}_n|, |\mathbf{F}_{dt}|\} \mathbf{t}_{ij} \tag{22}$$

with $\mathbf{F}_n = \mathbf{F}_e + \mathbf{F}_{dn}$ being the total normal force and $\mathbf{F}_{dt}$ the tangential dissipative force defined as

$$\mathbf{F}_{dt} = -2\gamma_t M_{ij} \mathbf{V}_t. \tag{23}$$

In Eqs. (22) and (23), μ_c is the Coulomb friction coefficient, $\mathbf{V}_t$ the tangential component of the relative velocity between particles i and j, $\mathbf{t}_{ij}$ the unit vector along $\mathbf{V}_t$, and γ_t the tangential damping coefficient. The sum of the three contributions introduced above yields the contact force experienced by particle i from collision with a single particle j:

$$\mathbf{F}_{cj} = \mathbf{F}_e + \mathbf{F}_{dn} + \mathbf{F}_t. \tag{24}$$

When multiple particles make contact with particle i, the total contact force is simply the sum of forces exerted on particle i by each neighbor j:

$$\mathbf{F}_c = \sum_j \mathbf{F}_{cj.} \tag{25}$$

To summarize, the contact force model features four parameters: two physical parameters e_n [or γ_n through Eq. (21)] and μ_c, and two numerical parameters k_n and μ_t. μ_c is a material property and is reliably measurable for any real material or couple of real materials. e_n is straightforward to measure for spheres, and more challenging to measure and interpret for cubes. k_n controls the maximum geometric overlap between two colliding particles. Finally, γ_t is most likely the most challenging parameter to assign a value to, and we simply take $\gamma_t = \gamma_n$. For more details regarding our DEM granular solver, i.e., Grains3D, the interested reader is referred to [52].

C. Simulations setup

For our particle-resolved simulations of cubes and spheres, we have selected two values of the Galileo number: namely, Ga = 70 and Ga = 160, and a single value of the density ratio $m = 2$.

TABLE I. Summary of the parameters used for PR-DNS of suspensions of cubes and spheres.

ϕ	Ga	$D/\Delta x$	L/D	AR	N_p
0.01	70	20	15	2	128
0.05	70	24	15	2	644
0.10	70	32	10	2	381
0.20	70	32	10	1	381
0.01	160	24	15	2	128
0.05	160	24	15	2	644
0.10	160	32	10	2	381
0.20	160	32	10	1	381

These chosen values correspond to steady oblique and steady vertical settling of a single cube and a single sphere at Ga = 70, respectively. At Ga = 160, on the other hand, a single cube settles in a helical path [41], while a single sphere settles obliquely [27,56]. A summary of the simulated cases together with their parameters are presented in Table I.

The simulations in the present study are performed in tri-periodic rectangular computational domains with horizontal edge lengths $L_x = L_y = L$ and vertical extents of $L_z = \{L, 2L\}$, depictions of which are provided in Fig. 2. The mean volumetric flux of the suspension in the z (i.e., gravity) direction is kept zero via a dynamically adjusted pressure drop at each time step. With N_p particles each occupying a volume of $v_p = \pi/6$, the corresponding solid volume fraction is given

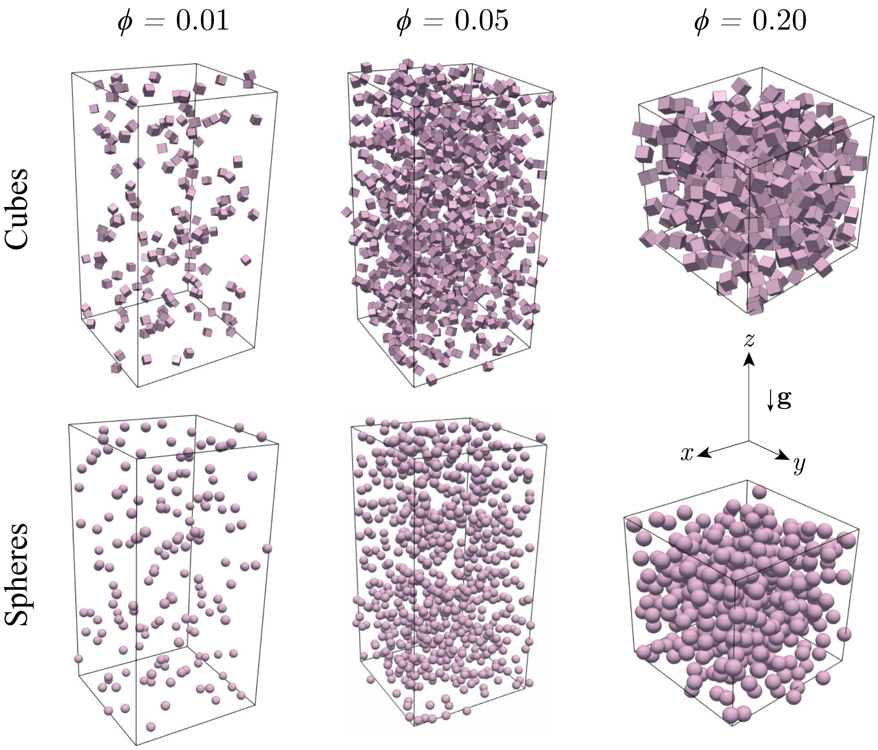

FIG. 2. Computational domains used for PR-DNS of cube and sphere suspensions with different volume fractions.

as $\phi = N_p v_p/(L^3 AR)$, where $AR = L_z/L_x$ denotes the aspect ratio of the domain. The length L and aspect ratio AR are chosen such that a balance is achieved between the sufficiency of the number of particles N_p for statistical analysis and the computational cost of the simulations. Another important consideration is the divergence of velocity fluctuations with the domain size [57]. At low Re, fluctuations grow linearly due to long-range hydrodynamic interactions. In contrast, it was shown that velocity fluctuations follow a much weaker logarithmic trend in randomly distributed dilute suspensions at finite Re [58] and in fact saturate to finite levels for Re $= O(10)$ [19]. This saturation is attributed to the inertial screening effect due to the formation of nonrandom microstructure in the suspensions [19,58]. For a dilute concentration of $\phi = 0.01$ at Re $= 50$, particle and fluid velocity fluctuations were reported to be insensitive to the domain size beyond 10 particle diameters [59]. Nevertheless, Uhlmann and Doychev [1] indicated in their analysis that while spatial autocorrelation values decline substantially for moderate separation distances (e.g., $20D$–$40D$), full decorrelation of vertical velocity signals is not achieved even for domain extensions as large as $L_z = 680D$ in sphere suspensions with $\phi = 0.005$ and Ga $= \{121, 178\}$. Considering the preceding discussion, for the cases with $\phi = \{0.01, 0.05\}$ the domain edge lengths are chosen to be $15D$ in the horizontal direction and elongated twice as much in the vertical direction. This is done in order to account for the particle wake anisotropy such that any spurious effects due to periodicity conditions are minimized.

Initial particle positions are obtained using a random number generation algorithm with a condition to prevent the occurrence of overlaps. We use the same set of contact force model parameter values for spheres and cubes. In all simulations, we set the restitution coefficient e_n to 0.75 and the Coulomb friction coefficient μ_c to 0.5, and we adjust the stiffness k_n so that the maximum dimensionless overlap between the particles, $\delta_{\max}/D$, is always less than 0.1%. Moreover, the granular time step is chosen such that $\delta t = (1/20)T_c$, with T_c being the contact duration [52], whereas the fluid time step is set to $\Delta t = (1/500)t_g$. The chosen Δt satisfies the Courant-Friedrichs-Lewy (CFL) condition of CFL < 0.2 for the grid resolutions listed in Table I. While in cases with $\phi = \{0.10, 0.20\}$, a pseudostationary state is attained and sustained long enough by running the simulations up to $1000t_g$, the less concentrated cases with $\phi = \{0.01, 0.05\}$ and Ga $= 160$ required to be run up to $\approx 2000t_g$ to reach and maintain a pseudosteady state for sufficiently long duration of time, such that reliable statistics could be collected.

III. RESULTS

In the following sections, all particle-related quantities are presented as ensemble-averaged values unless stated otherwise. Therefore, no particular notation is used for averaging operation over particles in the system. Time averaging, on the other hand, is denoted by angular brackets shown as $\langle \cdot \rangle$. Additionally, red lines and square symbols and black lines and circles in all plots are reserved for the data of cube and sphere suspensions, respectively.

A. Settling velocity

As discussed earlier in the Introduction, the settling velocity of a suspension is hindered mainly as a result of the upward flux of the fluid compensating for the downward motion of the particles. The Reynolds numbers based on the pseudosteady hindered settling rates are reported in Table II. Furthermore, Figs. 3(a) and 3(b) show hindered settling rates of cube and sphere suspensions, $\langle V_z \rangle$, normalized by the terminal velocity of the corresponding isolated particle, $\langle V_{z,s} \rangle$. For an isolated sphere, $\langle V_{z,s} \rangle$ is computed using the empirical relation available for Ga and Re$_t$ given in [11], and for a cube, we use the results from our previous study on the motion of a single cube [41]. As can be seen, the dependence of settling rate on the solid volume fraction for sphere suspensions is well described by Eqs. (2) and (3) when $\phi \geqslant 0.05$ in both Figs. 3(a) and 3(b). Note that in using Fig. 2, we have also incorporated the prefactor proposed by Di Felice [10] in Fig. 2 with a value of $k = 0.85$.

TABLE II. Terminal Reynolds numbers based on ensemble- and time-averaged settling velocities for all cases presented in Table I.

$\mathrm{Re} = \rho_f \langle V_z \rangle D/\mu$		$\phi = 0.01$	$\phi = 0.05$	$\phi = 0.1$	$\phi = 0.2$
Ga = 70	Spheres	64.7	53.7	43.3	30.0
	Cubes	56.8	44.4	35.6	23.8
Ga = 160	Spheres	228.1	160.9	127.9	89.7
	Cubes	172.1	123.3	98.9	68.1

For Ga = 70, both cube and sphere suspensions settle slower than an isolated particle at the same Ga as shown in Fig. 3(a), while cube suspensions are always somewhat slower than sphere suspensions. The situation is, however, different for Ga = 160. In the case of spheres, we find that the suspension with the lowest ϕ settles faster than an isolated sphere. Such a behavior has also been observed by Uhlmann and Doychev [1], where the settling velocity of the suspension with $(\mathrm{Ga}, \phi) = (178, 0.005)$ was reported to be 12% higher than a single sphere. In our case with $(\mathrm{Ga}, \phi) = (160, 0.01)$, the relative enhancement of settling velocity turns out to be approximately 7%. For cube suspensions, the choice of velocity scale for normalization of the settling rate affects the interpretation of the results, owing to the different dynamics of a single cube compared to a single sphere. Figure 3(c) shows three stages in the time evolution of the settling of a single cube in an unbounded fluid at Ga = 160 and $m = 2$. The cube initially settles at a relatively high velocity in a vertical path [denoted as “initial” in Fig. 3(c)], which is followed by the appearance of vortex shedding and rotational motion leading to significant deceleration (denoted as “transient” in Fig. 3(c)). Eventually, the cube establishes a sustained helical motion. If $\langle V_z \rangle$ for cube suspensions is normalized using $\langle V_{z,s} \rangle$ obtained from the initial stage of Fig. 3(c), we essentially see a trend similar to figure 3(a) at Ga = 160 [i.e., red squares in Fig. 3(b)]. On the other hand, using the final stage $\langle V_{z,s} \rangle$ of Fig. 3(c) results in higher values of $\langle V_z \rangle / \langle V_{z,s} \rangle$ for cubes compared to spheres [i.e., orange squares in Fig. 3(b)]. Moreover, the cube suspension with $\phi = 0.01$ is now seen to settle faster than a single cube at its final stage of motion. The reason for such a trend for $\phi = 0.01$ is twofold. First, the helical motion of a single cube, which requires a delicate balance of forces and torques acting on the cube, cannot be established and sustained in the presence of perturbations from nearby cubes. Consequently, such effective deceleration of the cube as in Fig. 3(c) does not conceivably occur.

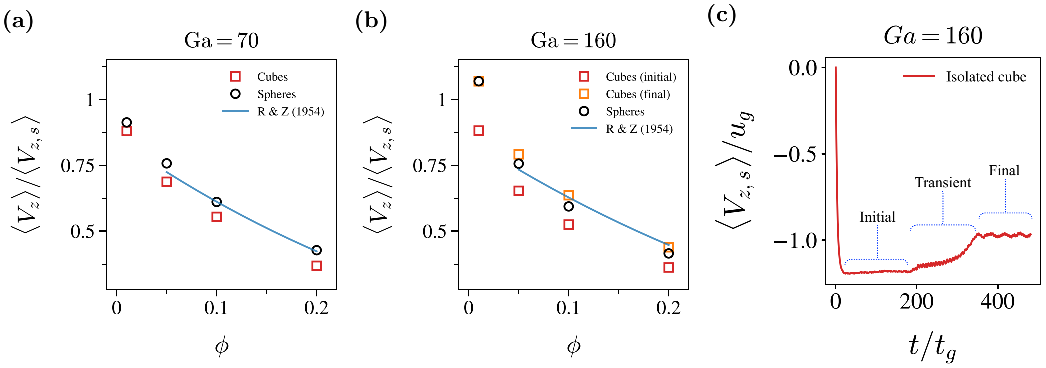

FIG. 3. Suspension settling velocities normalized by the terminal velocity of an isolated particle as a function of solid volume fraction for the two Galileo numbers of Ga = 70 and Ga = 160. The dashed lines in (a) and (b) show the Richardson and Zaki [6] formula presented in Fig. 2, with the prefactor $k = 0.85$. (c) The vertical velocity of an isolated cube as a function of time at Ga = 160 normalized by the gravitational velocity scale.

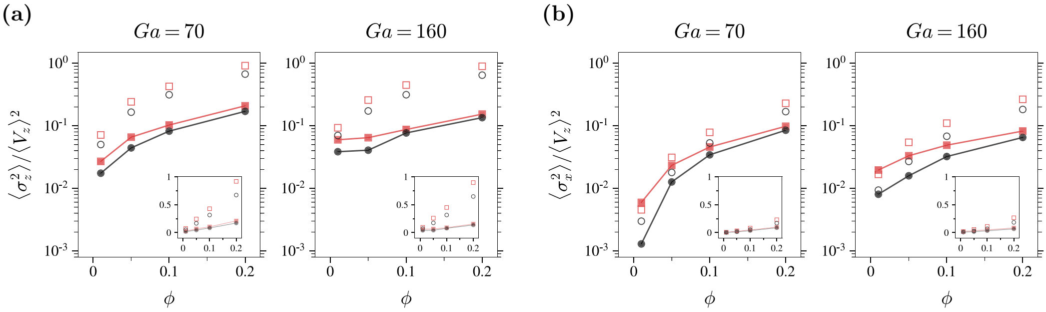

FIG. 4. Velocity fluctuations (a) in the gravity direction and (b) normal to the gravity direction. The particle and fluid data are shown by solid and open symbols, respectively, whereas red and black lines and symbols demonstrate the results for cube and sphere suspensions, respectively. The inset of each plot shows the same data on a linear scale.

Second, even though cubes are significantly more likely to break free from clusters compared to spheres as will be discussed in Sec. III D, there is still a considerable probability of finding a cube in the wake of another, which acts towards reducing the overall drag force experienced by the cube suspension.

B. Velocity fluctuations

Time-averaged values of particle and fluid velocity fluctuations of the cube and sphere suspensions, represented by velocity variance σ^2, are given in Fig. 4. Fluid fluctuations are obtained by computing the fluid velocity variance in a cubic control volume centered around each particle with an edge length of $4D$, excluding grid points lying inside the solids. Figures 4(a) and 4(b) show fluctuations in the gravity and normal directions, respectively. Moreover, time evolution of the same quantities are presented in Figs. 5 and 6. The variance values in all cases are normalized by the square of the corresponding settling rate of each suspension, which is the reason that the resulting quantity is occasionally referred to as "relative fluctuation" in the literature [19,60].

Overall, we find that the velocities of cube fluctuate with higher magnitude compared to spheres particularly in the transverse direction, and that the differences between cube and sphere suspensions in terms of particle fluctuation levels diminish as ϕ increases. In Fig. 4(a), particle fluctuations pertaining to the regime where $(\text{Ga}, \phi) = (160, 0.01)$ appear to be higher than might be expected. As will be highlighted in Sec. III D, strong columnar clustering occurs for both cube and sphere suspensions at this regime, which underlies the high values of vertical particle fluctuations as a result of prevalent DKT-type interactions. In Fig. 5, we observe more clearly that fluctuations of spheres in both directions remain almost the same upon increasing Ga, except for the most dilute of $\phi = 0.01$. For cubes, however, enhancement of fluctuations with Ga are seen up to $\phi = 0.05$, particularly in the horizontal direction. Moreover, cube suspensions at $(\text{Ga}, \phi) = (160, 0.01)$ and $(\text{Ga}, \phi) = (160, 0.05)$ exhibit long periods of high vertical velocity fluctuation, reminiscent of those observed by Willen and Prosperetti [16] for sphere suspensions. As particles interact more frequently at higher solid volume fractions, the magnitude of fluctuations increases with concentration for both types of particles, as seen in Fig. 4. While hydrodynamic interactions are mainly responsible for this increase at lower solid volume fractions, contact and collision between particles become more pronounced at higher ϕ, thus contributing greatly to the increase of particle velocity fluctuations.

For both types of particles, fluid velocity variances (shown with open symbols in Fig. 4) are significantly larger than that of particles for $\phi \geqslant 0.05$. For $\phi = 0.01$, the differences are smaller since particles are expected to better follow large-scale fluid motions in dilute regimes. In more concentrated cases, particles fail to adapt to smaller flow structures with length scales approximately

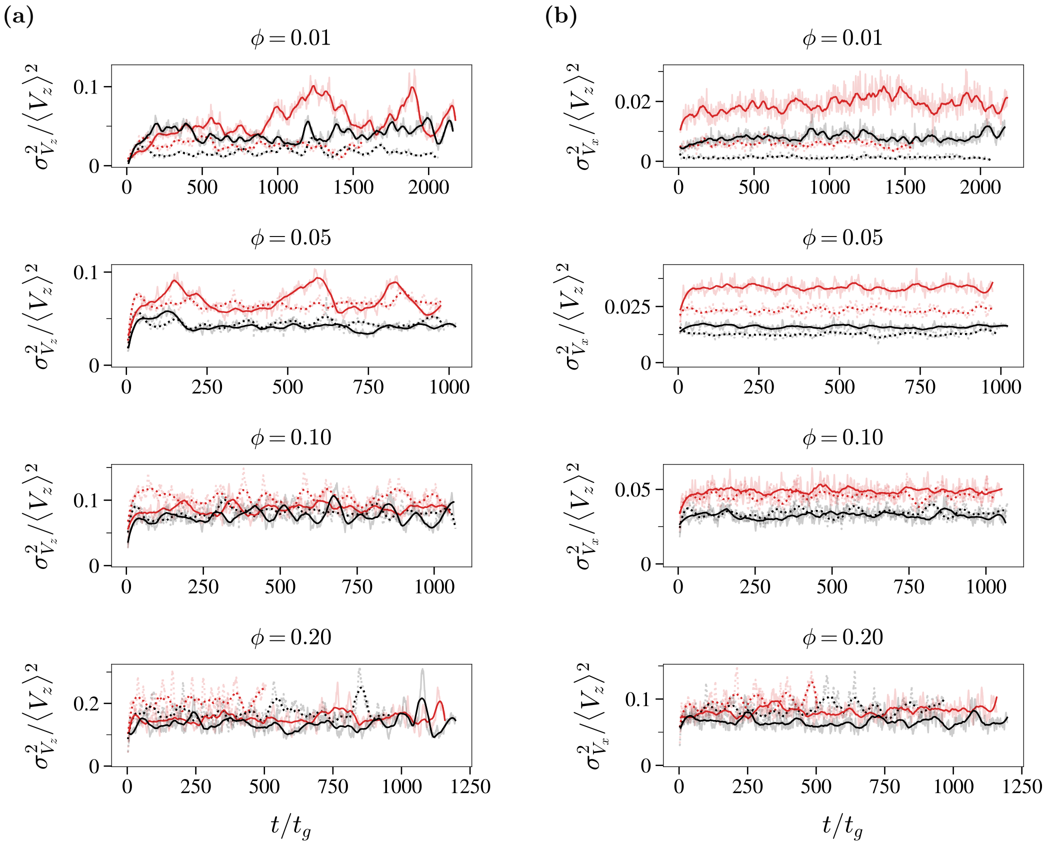

FIG. 5. Time evolution of (a) vertical and (b) horizontal particle velocity fluctuations. In these plots, red and black lines demonstrate the results for cube and sphere suspensions, respectively. Additionally, solid lines represent simulations with Ga = 160, whereas dotted lines show data for simulations with Ga = 70. In order to enhance visual representation of the plots, darker lines show a filtered version of the data, while the original data are plotted with a lighter color.

equal to D [58]. In general, the fluid pseudoturbulence induced by cubes is seen to be considerably higher than that of spheres. That is, on average, $\sigma^2_{u_z}/\langle V_z\rangle^2$ is 41% higher for cubes for both Galileo numbers, whereas $\sigma^2_{u_x}/\langle V_z\rangle^2$ is 52% and 72% higher for Ga = 70 and Ga = 160, respectively. For $\phi \geqslant 0.05$, vertical fluctuations are quite similar in their average values when Ga increases from 70 to 160 for both cubes and spheres. In contrast, cubes manifest large differences in the fluid velocity variance in the horizontal direction between Ga = 70 and Ga = 160 for all solid volume fractions, except $\phi = 0.2$. Sphere suspensions, on the other hand, do not experience such a dramatic amplification of fluctuations upon increasing Ga, except for the most dilute case.

Figure 7 shows the anisotropy of particle and fluid velocity fluctuations obtained from the ratio of vertical to horizontal components of velocity variance. The amplification of velocity fluctuations with solid volume fraction shown in Fig. 4 is also accompanied by a reduction in the level of anisotropy in all suspensions, consistent with results obtained for sphere suspensions in the literature [16,58,61]. More importantly, it is remarkable that the anisotropy of fluctuations in cube suspensions is always smaller than in sphere suspensions, whether it be for particle [Fig. 7(a)] or fluid [Fig. 7(b)] velocity fluctuations. This indicates that in cube suspensions, particle momentum and energy is more effectively transferred from the gravity to the transverse direction, thus making these suspensions

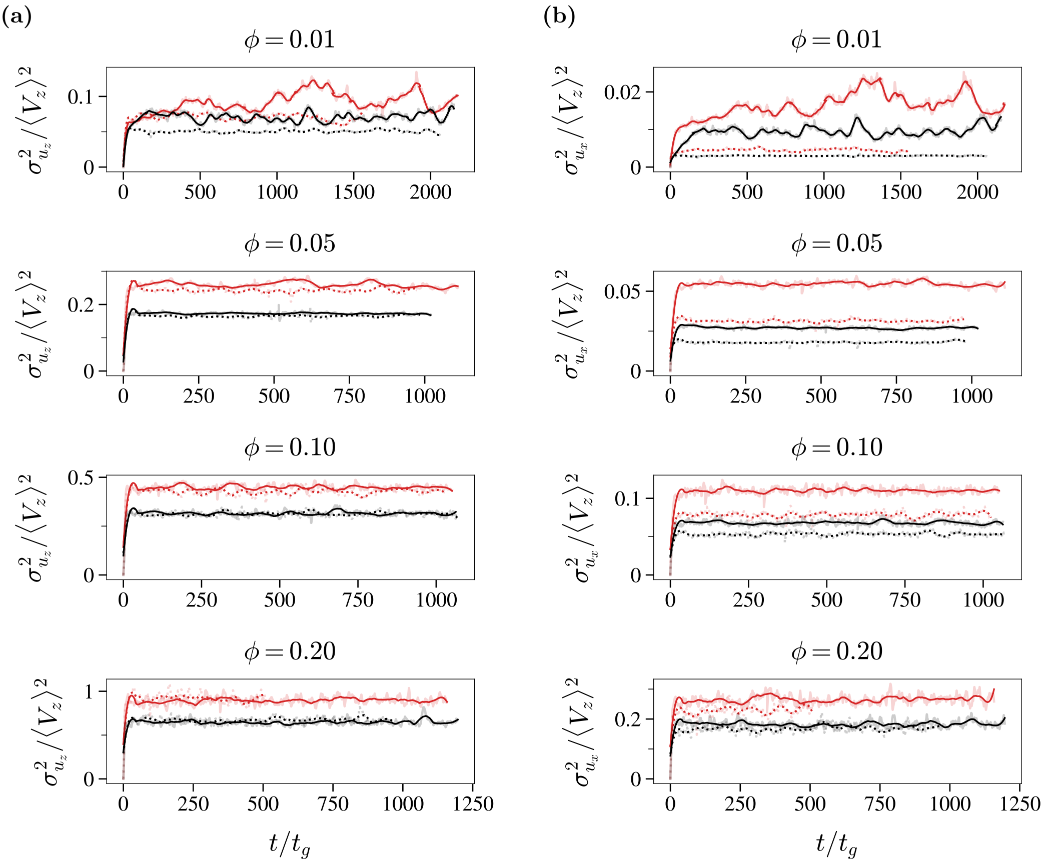

FIG. 6. Time evolution of (a) vertical and (b) horizontal fluid velocity fluctuations. Interpretation of line styles and colors is given in the caption of Fig. 5.

more isotropic. For the most dilute case with Ga = 70 in Fig. 7(a), anisotropy of particle velocity fluctuations is quite high for spheres due to the limited lateral motions at this regime, whereas the cube suspension is ≈50% more isotropic. The value of anisotropy in our sphere suspension is ≈12, which is close to the value of 12.96 reported by Yin and Koch [58] obtained for a suspension with

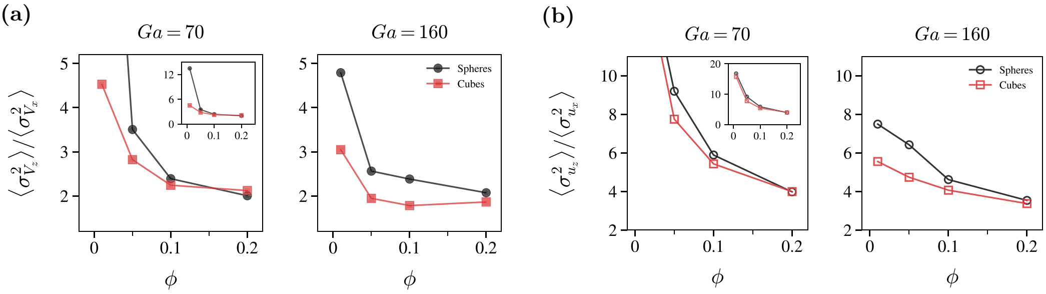

FIG. 7. Anisotropy of (a) particle and (b) fluid velocity fluctuations indicated by the ratio of the vertical to horizontal velocity variance. The insets show extended ranges of values on the vertical axis.

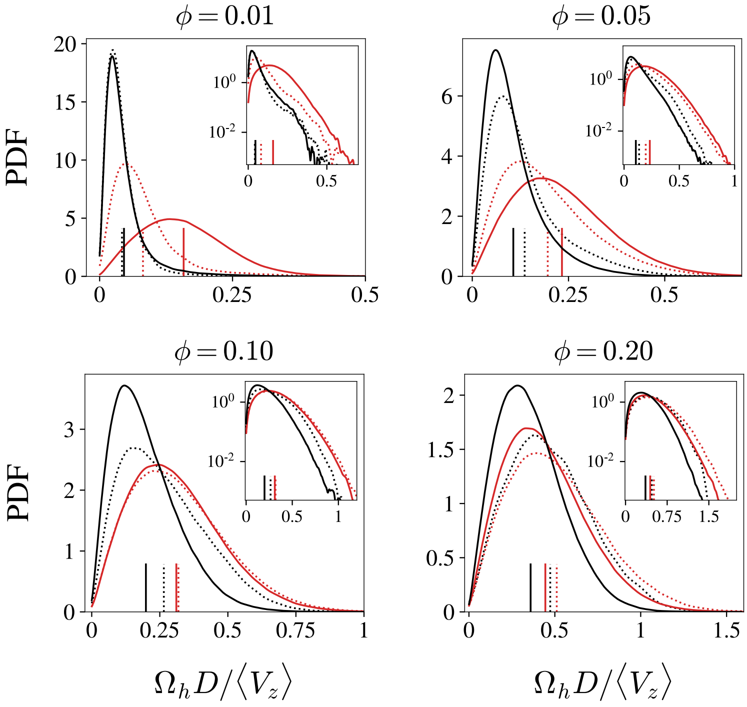

FIG. 8. Distribution of the horizontal component of particle angular velocities for different solid volume fractions. The insets show the same data with the y axis scaled logarithmically, while the mean value of each distribution is shown using short vertical lines on each plot. Interpretation of line styles and colors is given in the caption of Fig. 5.

$\mathrm{Re} = 10$. We also observe that increasing Ga renders almost all suspensions more isotropic due to the emergence and enhancement of transverse fluctuations. Furthermore, the differences between cube and sphere suspensions vanish for $\phi = 0.2$, meaning that both types of particles begin to behave similarly in terms of velocity fluctuations. Finally, studies that report values pertaining to the anisotropy of particle velocity fluctuations for sphere suspensions in regimes relevant to the present work are scarce. While Zaidi [61] obtained values of $\langle \sigma^2_{V_z} \rangle / \langle \sigma^2_{V_x} \rangle$ in the range of ≈ 5.7–6.76 for $0.05 \leqslant \phi \leqslant 0.2$, Willen and Prosperetti [16] report ≈ 1.2–1.7 for $0.087 \leqslant \phi \leqslant 0.262$. As it turns out, there is a large discrepancy between these two sets of values. Nevertheless, our results in Fig. 7(a) lie between those reported by others, albeit quite closer to the results of Willen and Prosperetti [16].

C. Angular velocities

In our previous study of the motion of an isolated cube [41], we found out that a cube rotates much more vigorously than a sphere at high Galileo numbers. This is due to the existence of sharp edges which induce strong hydrodynamic torques as the cube changes its orientation relative to the surrounding flow. In Fig. 8 distributions of horizontal angular velocities of particles, defined as $\Omega_h = \sqrt{\Omega_x^2 + \Omega_y^2}$, are plotted for the simulated suspensions. We choose to demonstrate the horizontal components, since it is this component that together with the vertical velocity of the particles generates the major contribution to the Magnus force in the horizontal direction. It is immediately obvious that in all cases, cubes not only exhibit higher angular velocities on average [e.g., up to ≈ 3 times higher for $(\mathrm{Ga}, \phi) = (160, 0.01)$], but are also more likely to experience more

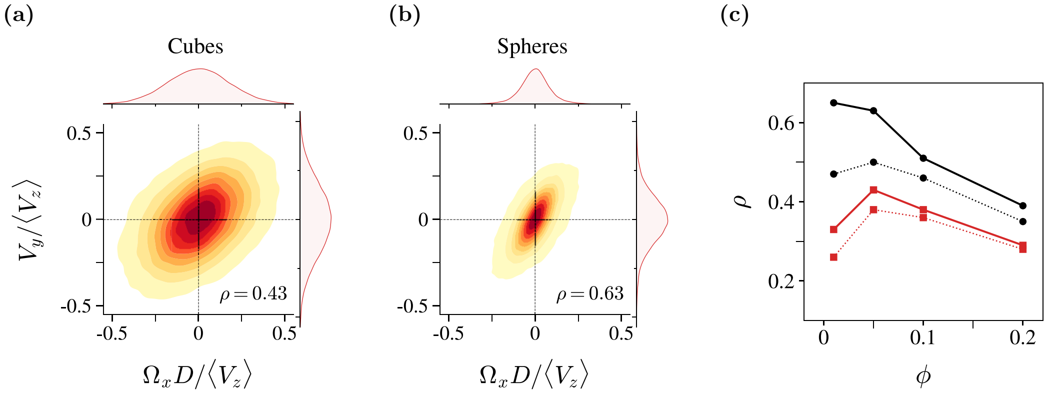

FIG. 9. Joint probability distribution functions of (a) cube and (b) sphere suspensions obtained for $(\mathrm{Ga}, \phi) = (160, 0.05)$, (c) Variation of Pearson's correlation coefficient as a function of the solid volume fraction for the simulated cases. Interpretation of line styles and colors is given in the caption of Fig. 5.

extreme values. Similar to velocity fluctuations, the differences become less pronounced with the increase in solid volume fraction, as interparticle contact and collisions begin to dominate particle kinematics. We can see that for $\phi = 0.01$ in Fig. 8, the distribution of angular velocities of spheres remains almost identical between $\mathrm{Ga} = 70$ and $\mathrm{Ga} = 160$, whereas for cubes there is a substantial shift towards higher Ω_h. This is similar to the case of an isolated cube, with the difference that an isolated cube at $\mathrm{Ga} = 70$ shows only negligible oscillations, while in a suspension of cubes the collective effect of the wake of the surrounding cubes induces considerable rotational motions. It can also be seen in Fig. 8 that the average magnitude of horizontal angular velocities for spheres turn out to be somewhat higher at $\mathrm{Ga} = 70$ compared to $\mathrm{Ga} = 160$, which might seem counterintuitive. However, the suspensions simulated here are by no means homogeneous, and as we will see in Sec. III D, the level of inhomogeneity increases with Ga. It leads us to presume that the reduction of angular velocities from $\mathrm{Ga} = 70$ to $\mathrm{Ga} = 160$ is a consequence of the stronger clustering of spheres at the higher Ga. One possible reason could be that since spheres at $\mathrm{Ga} = 160$ settle in larger groups, it is more probable for a sphere to be surrounded horizontally by neighboring spheres. It is thus more likely that the net microstructure-induced hydrodynamic torque attains smaller values at $\mathrm{Ga} = 160$ compared to $\mathrm{Ga} = 70$.

To further elucidate the influence of rotation on transverse forces and subsequent lateral motions, we present the joint probability distribution functions (JPDFs) of horizontal rotational and translational particle velocities in Fig. 9. Since the Magnus force is by definition directed along $\mathbf{V}_{\mathrm{slip}} \times \boldsymbol{\Omega} = (\mathbf{u} - \mathbf{V}) \times \boldsymbol{\Omega}$, the rotational velocity Ω_x is expected to give rise to a Magnus force and consequently a translational velocity in the positive y direction. Therefore, we consider JPDFs of Ω_x and V_y in Fig. 9, but similar information can also be equivalently obtained with Ω_y and V_x, with the only difference of the appearance of a negative correlation. In Fig. 9, ρ denotes the Pearson's correlation coefficient [62] defined as $\rho_{X,Y} = \mathrm{cov(X, Y)}/\sigma_X\sigma_Y$, which shows the covariance between two variables X and Y normalized by their standard deviations. The variation of ρ for both cube and sphere suspensions is given as a function of the solid volume fraction for $\mathrm{Ga} = 70$ and $\mathrm{Ga} = 160$ in Fig. 9(c). In all cases, ρ is expectedly found to be $\approx$0 for rotational and translational velocities in the same direction, e.g., Ω_x and V_x. We immediately notice in Fig. 9(c) that the normalized covariance is always stronger at $\mathrm{Ga} = 160$ than in $\mathrm{Ga} = 70$ for both types of suspensions, though more strongly so for spheres. Moreover, ρ is found to be consistently greater for spheres compared to cubes. We attribute this finding to the fact that unlike the case of a sphere, the rotation of a cube creates both a Magnus (i.e., rotation-induced) force and an orientation-induced lateral force [63]. Since the rotation of a cube is also accompanied by a change in its orientation, a constant rotation would create a lateral force that periodically changes sign. Therefore, even in the absence of the Magnus force, the rotation of a cube causes a sign-changing lateral force resulting in zero average covariance with velocity components. We speculate that this underlies the weaker correlation between rotational and translational velocity of cubes compared to spheres in Fig. 9(c). Additionally, the wider distribution of velocities in Fig. 9(a) compared to Fig. 9(b) is notable, implying that larger horizontal velocities are more frequently encountered in cube suspensions despite their weaker correlation with their rotational velocities. As signified by the less than perfect covariance of variables shown in Fig. 9(c), it should be emphasized that the rotational velocity of a particle and the corresponding forces are only partly responsible for its lateral motions. The other contributions include shear and vortex-induced as well as microstructure-induced lateral forces, which we investigated thoroughly in a previous work [22]. While rotation-, shear-, and vortex-induced forces are more influential in dilute regimes, microstructure-induced loads become increasingly more important in denser suspensions. An indication of this shift in relative importance is reflected by the decreasing covariance of rotational and translational velocities with solid volume fraction as shown in Fig. 9(c). Esteghamatian *et al.* [64] recently highlighted this point by demonstrating that in dense (e.g., $\phi \geqslant 0.4$) liquid-solid fluidized beds, neither Magnus nor Saffman forces contribute in any significant way to the lift force experienced by particles.

D. Microstructure

In order to characterize the microstructure of the simulated suspensions, we make use of the pair distribution function $P(\mathbf{r})$. This quantity shows the ratio of $\rho_n(\mathbf{r})$, the number density of neighboring particles in a volume ΔV located at $\mathbf{r}$, to $\overline{\rho_n}$, the average number density in the bulk of the suspension. In spherical coordinates, $P(\mathbf{r})$ is given as [65]

$$P(\mathbf{r}) = P(r, \theta, \psi) = \frac{\langle \rho_n(r, \theta, \psi) \rangle}{\overline{\rho_n}} = \frac{\langle H(r, \theta, \psi) \rangle}{\overline{\rho_n} \Delta v}, \tag{26}$$

where $\mathbf{r}$ is the pair separation vector pointing to the center of a neighboring particle given a reference particle at the origin $\mathbf{r} = \mathbf{0}$, θ the azimuthal angle measured from positive z axis, ψ the polar angle measured from positive x axis, ρ_n the average number density of particles in the computational domain, $\Delta v = r^2 \sin\theta \Delta r \Delta\theta \Delta\psi$ the volume element, and $H(r, \theta, \psi)$ the histogram of particle pairs. Since in our simulations, $P(r, \theta)$ is axisymmetric about the gravity direction, we compute only $P(r, \theta)$, which is $P(\mathbf{r})$ averaged over all values of ψ. To obtain $P(r, \theta, \psi)$, the space is first discretized with $\Delta r = 0.1D$ and $\Delta\theta = \pi/60$. At each sampling time, we create periodic and multiperiodic images of the particle positions, followed by a loop for each particle and over the surrounding space to count the number of neighbors happening to be in the subvolume Δv at any given r and θ. The histogram $H(r, \theta)$ is thus progressively constructed, and finally averaged over at least 3000 time snapshots for each case. Another informative quantity can also be derived from Eq. (26) by averaging $P(r, \theta)$ over θ, yielding the radial distribution function

$$g(r) = \frac{1}{2} \int_0^{\pi} P(r, \theta) \sin\theta \, d\theta, \tag{27}$$

which shows the ratio of the number density in a spherical shell with thickness Δr a distance r away from the reference particle to the bulk number density, regardless of the relative orientation.

The pair and radial distribution functions are plotted for Ga = 160 and Ga = 70 in Figs. 10 and 11, respectively. The color bars have been set to represent the same range of values for all cases so that direct comparisons can be made. The strong clustering of particles in the vertical direction for the sphere suspension at $(\mathrm{Ga}, \phi) = (160, 0.01)$ in the form of a columnar structure is the most remarkable feature of the pair distribution functions in Fig. 10. Such a prominent vertical clustering of spherical particles has also been reported by Uhlmann and Doychev [1] at $(\mathrm{Ga}, \phi) = (178, 0.005)$, and later confirmed experimentally by Huisman *et al.* [18]. In Fig. 10 we also note an increased concentration of spheres in the horizontal direction relative to the reference particle. Interestingly,

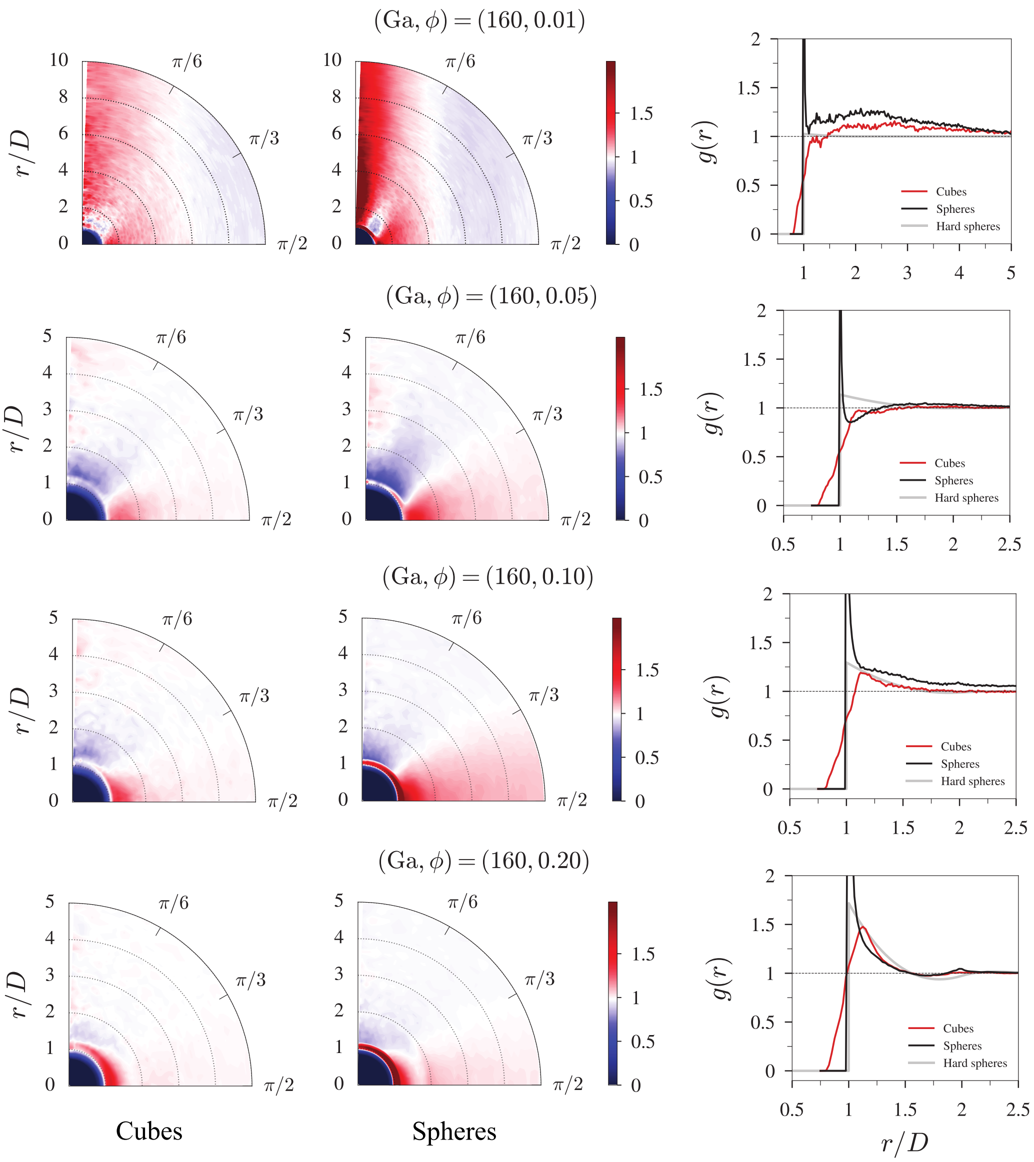

FIG. 10. Pair and radial distribution functions obtained for microstructure characterization of suspensions at Ga = 160. The leftmost and center columns in the figure pertain to cube and sphere suspensions, respectively. On the rightmost plots, radial distribution functions of hard spheres [66] are also given as a reference in addition to those obtained from the suspension simulations.

this was also observed by Uhlmann and Doychev [1], despite the fact that their simulated suspension was more dilute and the Galileo number that they used was slightly higher. The formation of these horizontal configurations was attributed to the tumbling phase of the well-known DKT phenomenon. Conversely, while the cube suspension in the same regime, i.e., $(\mathrm{Ga}, \phi) = (160, 0.01)$ also exhibits increased concentration in the vertical direction, it is obvious that the intensity of clustering is significantly smaller than what is seen for the sphere suspension. The pair distribution function for the cube suspension at $(\mathrm{Ga}, \phi) = (160, 0.01)$ is seen to be more uniformly distributed, sharing some

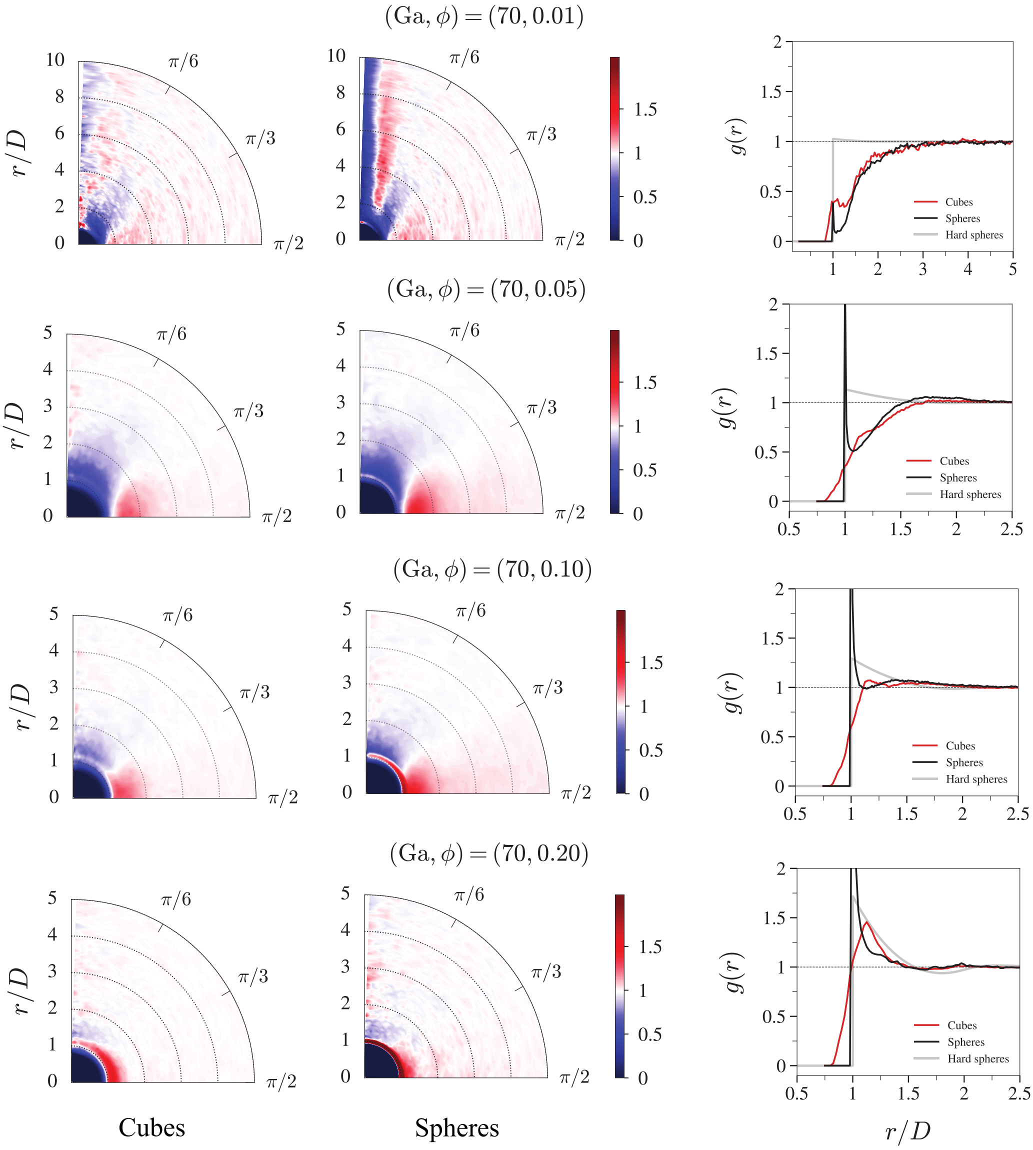

FIG. 11. Pair and radial distribution functions obtained for microstructure characterization of suspensions at Ga = 70. The leftmost and center columns in the figure pertain to cube and sphere suspensions, respectively. On the rightmost plots, radial distribution functions of hard spheres [66] are also given as a reference in addition to those obtained from the suspension simulations.

similar qualities as well. For both suspensions, we find that the radial distribution function attains significantly larger values compared to a hard-sphere distribution [66]. Furthermore, for all solid volume fractions shown in Fig. 10, a sharp peak is persistently observed for sphere suspensions. Inspection of pair distribution functions reveals the existence of a "contact rim," i.e., a circular high-density band, at $r/D = 1$ for all sphere suspensions (though somewhat weaker in the case of $\phi = 0.05$). This region exists as spheres spend a relatively long time in contact with each other during the tumbling phase of DKT. Obviously, this point of contact is always located at $r/D = 1$

for spheres which causes the sharp peak at $r/D = 1$, whereas for cubes, contact can occur at any center-to-center distance in the range $\sqrt{\pi/6} \leqslant r/D \leqslant \sqrt{\pi/2}$ due to its geometry. This is evident from radial distribution functions of cubes appearing as approximately oblique lines about $r/D = 1$. At higher solid volume fractions, the wakes of particles become much more frequently disrupted by their neighbors. Additionally, the settling Reynolds number also decreases with increasing ϕ due to the stronger hindrance effect for the same Ga (as noted in Table II), leading to weaker particle wakes. This is why the prominent vertical configuration of particles at $\phi = 0.01$ quickly fades away upon increasing the suspension concentration, even though there still remains weak traces of vertical accumulation for both cube and sphere suspensions at $(\mathrm{Ga}, \phi) = (160, 0.05)$. Since the vertical arrangement of particles is unstable, both spheres and cubes quickly tumble into stable horizontal configurations, leading to a deficit in the vertical direction of the pair distribution functions. This is reflected quite clearly for sphere suspensions in the form of high-density horizontal regions. In the case of cubes, while the same horizontal structures can still be detected in almost all cases, not only the pair distribution functions are much fainter, but also the horizontal extension of these regions are significantly more limited. This observation is also confirmed by the reduced magnitude of the radial distribution functions for cube suspensions compared to their sphere counterparts. Notably, the pair distribution function of the cube suspension for $(\mathrm{Ga}, \phi) = (160, 0.20)$ in Fig. 10 is almost uniform except for $r/D \leqslant 2$, whereas the extended light blue and red regions and their margin is still clearly discernible in the sphere suspension. We will demonstrate in Sec. III E that this particular difference in microstructure is, at least partly, responsible for the differences observed in the drag force experienced by cube and sphere suspensions. While at relatively low solid volume fractions the suspensions are markedly inhomogeneous, the microstructure shows resemblance to random distributions (i.e., hard-sphere distributions in the case of sphere suspensions, and their equivalent for cube suspensions) at $\phi = 0.2$, as many-body interactions begin to dominate the dynamics of the suspensions.

At a lower Galileo number of $\mathrm{Ga} = 70$, we conversely find a strong deficit of particles in the vertical direction near the reference particle for both sphere and cube suspensions, especially in the most dilute case. Comparison of radial distribution functions reveals that except for $\phi = 0.20$, this deficit is remarkably more pronounced compared to suspensions at $\mathrm{Ga} = 160$. We also find that the pair distribution functions for both sphere and cube suspensions at $(\mathrm{Ga}, \phi) = (70, 0.01)$ are starkly different from those obtained for $(\mathrm{Ga}, \phi) = (160, 0.01)$. In Fig. 11, a slender vertical region depleted of particles is visible for the sphere suspension at $(\mathrm{Ga}, \phi) = (70, 0.01)$, which is the complete opposite of our observation for $(\mathrm{Ga}, \phi) = (160, 0.01)$. From Fig. 11, it can be seen that this low concentration region is immediately adjacent to a higher concentration region. More importantly, such a well-defined depletion zone cannot be detected in the case of the cube suspension at $(\mathrm{Ga}, \phi) = (70, 0.01)$, although weak signs of vertical voids are visible. Another notable observation is that in contrast to sphere suspensions at $\mathrm{Ga} = 160$, the contact rim does not appear as strongly at $\mathrm{Ga} = 70$. This means that while particles undergo DKT, they either do not touch as frequently, or spend as much time in contact even if they do. Correspondingly, the peaks of the radial distribution functions of sphere suspensions are higher and wider at $\mathrm{Ga} = 160$ compared to $\mathrm{Ga} = 70$. For the highest solid volume fraction of $\phi = 0.20$, while cube suspensions have an almost uniform pair distribution function for separation distances greater than $r/D = 2$, the horizontal sector of higher particle concentration is still distinguishable in the sphere suspension at $\mathrm{Ga} = 160$ and $\phi = 0.20$.

In order to demonstrate the microstructure evolution, we also present in Fig. 12 the ensemble-averaged local solid volume fraction ϕ_{loc}. This quantity is obtained by considering a cubical control volume of edge length $4D$ centered on the location of each particle, and then computing the ratio of the number of grid points lying in the solid objects to the total number of points inside that control volume, and then performing ensemble averaging at each time step. It is noted that although this method inevitably results in a pixelated (i.e., stepwise) representation of the particles, it still yields a reliable estimation of the local solid volume fraction for comparison purposes. Despite the overall similarity of pair distribution functions of cubes and spheres for $\phi \geqslant 0.05$ presented in Figs. 10 and

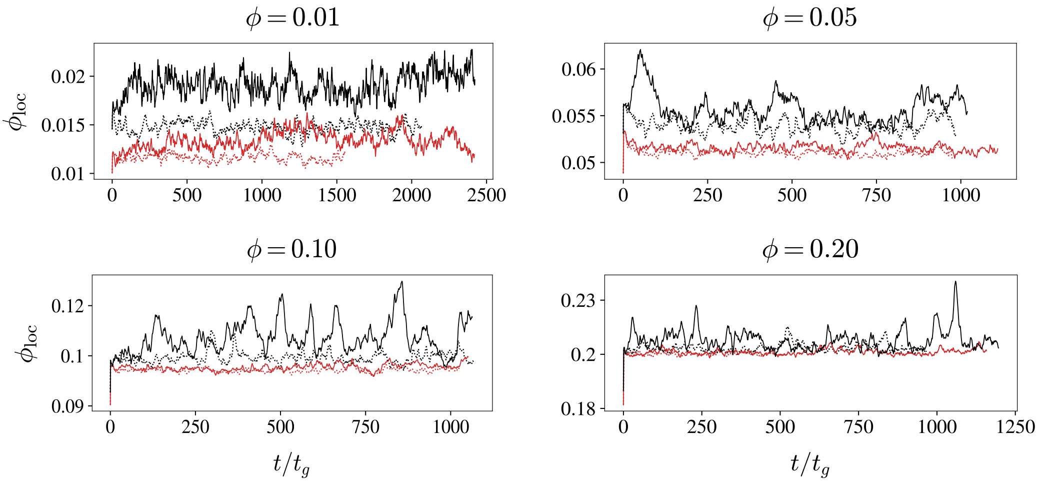

FIG. 12. Time evolution of ensemble-averaged local solid volume fraction ϕ_{loc}. Interpretation of line styles and colors is given in the caption of Fig. 5.

11, the local solid volume fraction in sphere suspensions undergoes several high peaks that last for long periods of time, particularly at Ga = 160. In contrast, such noticeable peaks are not seen in the values of ϕ_{loc} for cube suspensions. Moreover, the plots in Fig. 12 unequivocally show that spheres are always locally closer to each other than cubes. For $\phi \geqslant 0.05$, there is a distinctive change in values of ϕ_{loc} in sphere suspensions when increasing Ga from 70 to 160, while for cubes the only noticeable change appears to be in the most dilute case with $\phi = 0.01$. We believe that the high peaks seen for sphere suspensions correspond to the persistent contact rim seen in Figs. 10 and 11 (and equivalently the sharp peaks of the radial distribution functions), and hence exist due to the fact that at Ga = 160 spheres spend a substantial amount of time in the kissing phase of DKT. Since the contact rim also exists, although not as prominently, for Ga = 70 as well, we conclude that at Ga = 160 a greater number of particles should be in direct contact to explain the appearance of high values of local solid volume fraction shown in Fig. 12.

The preceding descriptions of the microstructure of simulated systems confirm that inertial liquid-solid suspensions of spheres and cubes are nonrandom, particularly for lower solid volume fractions. It also turns out that the hydrodynamics of dilute suspensions can be very different at Ga = 70 and Ga = 160, an example of which is the narrow vertical depletion region of sphere suspensions at $(\mathrm{Ga}, \phi) = (70, 0.01)$ (Fig. 11) as opposed to the high concentration column of spheres at $(\mathrm{Ga}, \phi) = (160, 0.01)$ (Fig. 10). At the higher Galileo number of Ga = 160, the wake is strong enough to attract particles from relatively long distances. As noted in [1], an isolated sphere settles steadily along an oblique path at this Galileo number, which might be a contributing factor in leading particles into the wake region of another particle. The trapped spheres spend a sufficiently long time in the formed clusters such that a substantial imprint is left on the pair distribution function of their corresponding suspension. These particles then collide with the leading particle, and tumble into a horizontal position. At the lower Galileo number of Ga = 70 and for $\phi = 0.01$, however, spheres get repelled from the wake region. We suspect that due to the existence of shear in the wake, particles experience a lift force that effectively pushes them away from the wake region. Interestingly, Kurose and Komori [67] have shown that the lift force exerted on an isolated sphere in shear flow acts towards the higher velocity region for $\mathrm{Re} < 60$, and in the opposite direction for $\mathrm{Re} > 60$ due to flow separation at higher Re. Their finding seems to reinforce our conjecture of particles getting repelled from the wake region by the shear-induced lift at Ga = 70, while being attracted to the wake of another particle at Ga = 160. In both of these scenarios, cube suspensions are considerably more homogeneous. In our previous study of the free motion of an isolated cube [41], we have shown that a cube experiences much larger rotation rates and transverse forces (e.g., Magnus force) due to its geometry compared to a sphere. A slight change in the orientation of a cube can induce significant hydrodynamic torques and subsequent rotations. Even though the helical motion of an isolated cube at $\mathrm{Ga} = 160$ is unlikely to be sustained in the presence of other cubes, the inherent susceptibility of cubes to rotation is still very likely to cause significant side motions. This is why we suggest that the less pronounced clustering of cube suspensions originates from high rotational velocities of cubes, which consequently enhances their chances of effectively escaping clusters. This conclusion is also in line with the results of Kajishima [68] in PR-DNS of dilute sphere suspensions at high Reynolds numbers, which indicated that irrotational spheres maintain cluster structures whereas rotational spheres in contrast tend to cause periodic break-up of clusters.

E. Drag force

Prior to presenting the numerical results, it is necessary to stress that in the literature, two different quantities have been referred to as the drag force; namely, the total drag and the flow-induced drag denoted by $\mathbf{F}$ and $\mathbf{F}_d$, respectively. In a suspension system where a static macroscale pressure gradient exists, the total drag force acting on a particle is the sum of a buoyancy-type force $-v_p\nabla P$ (which is experienced even in the absence of a flow) and the flow-induced interaction force $\mathbf{F}_d$. The net drag force exerted on all particles is balanced by the pressure drop over the whole system such that

$$-V\nabla P = N_p\mathbf{F} = N_p(-v_p\nabla P + \mathbf{F}_d), \tag{28}$$

where V is the total volume of the system. From the above equation, it follows that $-v_p(1-\phi)\nabla P = \phi\mathbf{F}_d$, and therefore

$$\mathbf{F} = \frac{1}{1-\phi}\mathbf{F}_d. \tag{29}$$

In the present study, we have chosen to report the magnitude of the total drag force $\mathbf{F}$ for our results, which is the quantity that is directly computed by integrating hydrodynamic stresses in the simulations as in Fig. 10.

Several drag correlations have been proposed in the past for suspensions of spheres for varying ranges of Re and ϕ. However, the systems from which these correlations have been extracted have not always been similarly set up. The earliest drag correlation is the one proposed by Wen and Yu [69] based on fluidization experiments with the following form:

$$\frac{F}{F_s} = (1-\phi)^{-\beta-1}, \tag{30}$$

where F_s is the drag force of a single stationary sphere, for which reliable correlations exist [70,71]. Equation 30 is in fact the same relation that represents the dilute part of the drag correlation proposed by Gidaspow [72]. Wen and Yu [69] suggested that the exponent β is constant with a value of $\beta = 3.7$ over the entire range of Reynolds numbers, based on the observation that β turned out to be almost the same for the extremities of the Reynolds number range. Based on the available experimental data, Di Felice [73] later found that for the intermediate range of Re, β is a weak function of the Reynolds number obeying the following relation:

$$\beta = 3.7 - 0.65\exp\left[-\frac{(1.5-\log_{10}\mathrm{Re})^2}{2}\right], \tag{31}$$

where β goes through a minimum of $\beta \simeq 3$ for $20 \leqslant \mathrm{Re} \leqslant 80$. Due to obvious practical limitations, fixed-bed data such as those proposed by Ergun [74] can be obtained only for a highly concentrated system close to packing solid volume fractions. In recent years, the availability of massive

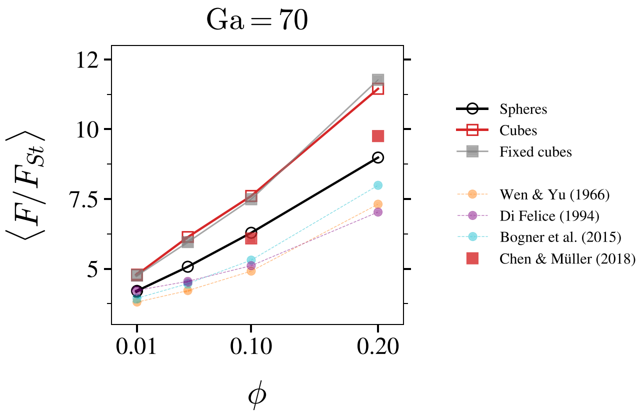

FIG. 13. Drag force of the cube and sphere suspensions as a function of solid volume fraction for two Galileo numbers of Ga = 70 and Ga = 160. Open and solid symbols represent data for dynamic suspensions and static beds, respectively. Along with the data obtained from the present PR-DNS, we also show the drag correlations proposed by Wen and Yu [69], Di Felice [73], and Bogner *et al.* [79] for spheres, and that of Chen and Müller [81] for fixed beds of cubes.

computational power has provided the opportunity to model fluid flow in fixed arrays of spheres over extended ranges of solid volume fractions and Reynolds numbers. The PR-DNS of Hill *et al.* [75,76], Beetstra *et al.* [77], Tang *et al.* [78], and Bogner *et al.* [79] based on lattice-Boltzmann method and that of Tenneti *et al.* [80] based on the immersed boundary method have provided correlations for drag force over stationary arrangement of spheres for dense systems (i.e., $\phi \geqslant 0.1$) and Reynolds numbers mostly up to Re = 300. Of particular relevance to the present work is the PR-DNS study of Chen and Müller [81] on the drag force of assemblies of cubic particles. In their study, super-quadric cubes were used (having relatively round corners and edges) to obtain a drag correlation for $0 \leqslant \mathrm{Re} \leqslant 200$ and $0.1 \leqslant \phi \leqslant 0.45$.

The drag force data collected from the present simulations are shown in Fig. 13, where the values are normalized by the Stokes drag relation $F_{St} = 3\pi\mu D\langle V_z\rangle$. On the same graphs in Fig. 13, we also show values of drag computed using correlations reported in the literature for spheres, and using the aforementioned correlation proposed for cubes [81] with parameters corresponding to our simulations. It should be pointed out that while the correlation of Bogner *et al.* [79] gives the total drag as given in Eq. (29), those proposed by Wen and Yu [69], Di Felice [73], and Chen and Müller [81] originally provide the flow-induced drag only, hence necessitating the multiplication by a factor of $1/(1-\phi)$ in order for comparisons to be made with our drag data in Fig. 13. Since these correlations require the Reynolds number (instead of the Galileo number) as an input, we use the Reynolds number based on the pseudosteady settling rate of the suspension in each simulation shown in Table II. In doing so, it should be noted that for correlations derived from fixed-bed systems, the Reynolds number based on superficial velocity is equivalent to the Reynolds number computed with the average settling velocity of the particles (relative to a fixed container) in sedimenting suspensions [11].

From Fig. 13, we can immediately recognize a number of distinct features. The most notable is the atypically lower drag experienced by both spheres and cubes at $(\mathrm{Ga}, \phi) = (160, 0.01)$ compared to their fixed-bed counterparts. As illustrated in Sec. III D, this is due to the formation of fast-settling clusters in this particular regime. In addition to the lower drag compared to fixed beds owing to the inhomogeneous microstructure, it turns out that both suspensions at $(\mathrm{Ga}, \phi) = (160, 0.01)$ on average settle faster even than an isolated particle according to the data in Table II. At this Galileo number and density ratio, a single sphere settles rectilinearly with a terminal Reynolds number of $\mathrm{Re} \simeq 213$, while a single cube significantly decelerates after an initial vertical motion and eventually settles in a helical path at Re $\simeq 155$ [41] [see also Fig. 3(c)]. While the higher-than-normal settling rate or equivalently the lower drag in dilute sphere suspensions have been lately reported by other researchers [1,18], we find that to be also true for a cube suspension at $(\mathrm{Ga}, \phi) = (160, 0.01)$, which appears to experience less drag compared to a fixed bed of cubes. Remarkably, no such drag reduction is observed for the similar solid volume fraction at Ga $= 70$. Another feature of Fig. 13 is that while the drag of sphere suspensions is higher than fixed beds of spheres except for $(\mathrm{Ga}, \phi) = (160, 0.01)$, the drag curve of cube suspensions closely follows the drag data of fixed beds of cubes in all cases, with the only exception of the case with $(\mathrm{Ga}, \phi) = (160, 0.01)$. Note that Fig. 13 shows two sets of drag data for fixed beds of cubes. One set, shown by solid gray squares, pertains to the simulations we performed with random cube arrangements at the same Reynolds numbers as the dynamic cases. The other set, represented by solid red squares, shows the drag of fixed beds of rounded super-quadric cubes obtained by Chen and Müller [81]. As can be seen, our drag values lie well above those reported in [81]. This discrepancy might have appeared at least partly owing to the fact that the cubes in our simulations are represented with sharp edges and corners, while the super-quadric cubes in [81] have a fair degree of roundness.

The similarity between the drag values of stationary and moving cube suspensions is rather surprising. One might expect moving cubes to experience a larger overall drag due to stronger velocity fluctuations, as is the case for an isolated moving cube compared to a fixed one. However, we believe that this trend may be justified by realizing that the relative magnitudes of factors contributing to the alteration of drag may be different for cubes and spheres. In general, the drag acting on mobile particles in a dynamic suspension would be different compared to the drag obtained from a stationary array (i.e., a fixed bed) of particles. The effect of particle motion on drag in suspensions has been a long-standing challenge for developing accurate drag correlations, as touched upon in the review article by Di Felice [82], and investigated by Tang *et al.* [83] and recently by Tavanashad *et al.* [21].

The difference between the drag of dynamic versus static suspensions stems from three factors; namely, suspension microstructure, velocity fluctuations and particle mobility. First, when particles are free to move, they show a preference for particular arrangements that are markedly different from a random (i.e., hard-sphere) distribution, as discussed previously in Sec. III D. These nonrandom structures develop as a result of interparticle hydrodynamic interactions such as DKT, leading either to clustering or dispersion [1,11,16], whereas dynamic gas-solid systems retain their random particle distributions on length scales of the order of the particle diameter [83,84]. Since cubes are found to be less likely to remain in clusters, the extended horizontal accumulation that enhances drag in the case of spheres is extremely weak in cube suspensions, if detectable at all (e.g., see Fig. 10). In order to demonstrate this point more clearly, we present broader views (i.e., up to $r/D = 8$) of the pair distribution functions in Fig. 14 for two solid volume fractions of $\phi = 0.1$ and $\phi = 0.2$, respectively. As evident in Figs. 14(a) and 14(b), high-density sectorial regions between $\pi/3 \leqslant \theta \leqslant \pi/2$ can be found in sphere suspensions at Ga $= 160$ even in the densest suspension, extending all the way up to $r/D = L_x$. In cube suspensions, though, any horizontal accumulation of neighbors is hardly seen beyond $r/D = 2$. These observations indicate that in cube suspensions, there is a considerably lower probability of finding neighbors oriented horizontally compared to sphere suspensions. The sharp peaks in radial distribution functions, together with high-density horizontal regions in cases with $\phi \geqslant 0.05$ and both Galileo numbers (evident in Figs. 10 and 11), and consequently the time evolution of local solid volume fraction in Fig. 12, overall point to the fact that spheres cling to one another horizontally for long periods of time. This behavior, which is not observed as prominently in cube suspensions, significantly amplifies the drag experienced by spheres.

Second, particle velocity fluctuations create additional shear in the flow and also introduce unsteady effects such as history and added-mass forces, which would otherwise be absent in a suspension with frozen particles. In Sec. III B, we presented particle velocity fluctuations for the present simulations. Even though the velocity variances are generally higher for cubes compared to spheres, the differences are most striking in the transverse direction and for more dilute cases.

(a) $\phi = 0.1$

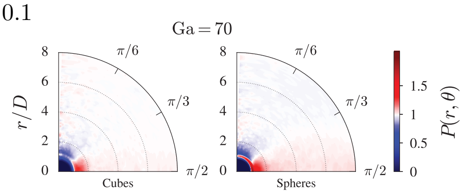

(b) $\phi = 0.2$

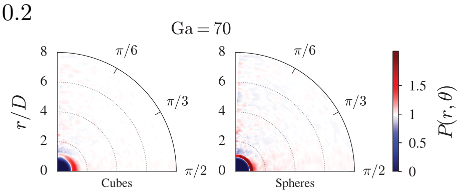

FIG. 14. Pair distribution functions of cube and sphere suspensions with extended ranges of the radial distance compared to Fig. 10 and Fig. 11. The plots pertain to cases with Galileo numbers of $\mathrm{Ga} = 70$ and $\mathrm{Ga} = 160$ and solid volume fractions of $\phi = 0.1$ and $\phi = 0.2$.

Moreover, Tavanashad *et al.* [21] noted that while in homogeneous suspensions higher fluctuations enhance the drag, this is not necessarily true for clustered suspensions.

Third, the ability of particles to adapt to flow changes is found to reduce drag in sphere suspensions, as demonstrated by Rubinstein *et al.* [85] for Stokes regime and Tavanashad *et al.* [21] for high Reynolds numbers. The mobility of particles is usually characterized in terms of the Stokes number given as $\mathrm{St} = m\mathrm{Re}/18$, which is the ratio of particle momentum response time to the flow characteristic time. Two limiting cases of $\mathrm{St} \to 0$ and $\mathrm{St} \to \infty$ thus correspond to tracer particles adapting instantaneously to the flow and stationary particles in fixed beds, respectively. For the present liquid-solid suspensions, the Stokes number lies in the ranges of $10 \leqslant \mathrm{St} \leqslant 25$ for spheres and $8 \leqslant \mathrm{St} \leqslant 18$ for cubes. Although we did not study the effect of mobility of cubes on their drag, we speculate that the freedom of cubes to translate and rotate in response to the flow field variations should have a greater influence towards the reduction of drag compared to similar mobility effects in sphere suspensions [21], hence explaining the lower-than-expected drag of dynamic cube suspensions. The lower drag might also be linked to the orientation of each individual cube, which can on average be such that a nearly face-normal orientation occurs more frequently in a dynamic suspension than a completely random orientation in a fixed bed of cubes. Nevertheless, mobility and its ensuing effects in cube suspensions certainly need further specifically targeted investigations in order to firmly establish the mechanisms underlying the drag data trend seen in the results of this section.

IV. DISCUSSION AND FINAL REMARKS

In this investigation, we have simulated monodisperse liquid-solid suspensions of cubes and spheres with a solid-to-fluid density ratio of $m = 2$, for two Galileo numbers of $\mathrm{Ga} = 70$ and $\mathrm{Ga} = 160$ and a range of solid volume fractions of $0.01 \leqslant \phi \leqslant 0.2$. Through detailed microstructure analysis, we have found that while suspensions of cubes bear qualitative structural similarity to sphere suspensions, cubes appear to be less likely to stay in clusters. In line with this observation, we have shown that horizontal particle velocity fluctuations are significantly higher in cube suspensions due mainly to their susceptibility to stronger transverse forces; namely, orientation-induced forces and Magnus effects resulting from comparably high angular velocities. At the highest Galileo number of $\mathrm{Ga} = 160$ and the most dilute case of $\phi = 0.01$, we found long vertically aligned particle clusters standing out remarkably in sphere suspensions, but less conspicuously in cube suspensions. These columnar structures as well as the observed horizontal clusters arise due to the occurrence of the DKT mechanism. While the columnar arrangement quickly fades away with the increase of solid volume fraction owing to frequent wake disruptions by nearby neighbors, horizontal clusters persist in all concentrations. In contrast, there is a remarkable depletion of spheres in the wake of a reference sphere for $\mathrm{Ga} = 70$ and $\phi = 0.01$, which we attribute to a repelling lift force induced by the wake shear region [67]. In all cases, preferential concentration is unanimously less intense in cube suspensions, whether it be an accumulation or a deficit of particles in a certain region. In a sense, one may conclude that cube suspensions remain more homogeneous or better mixed. Such a conclusion bears important practical implications in real-life applications of particle-laden flows. As an example, in situations where particle agglomeration is to be avoided in order to enhance mixing or maximize surface transfer properties, angular shapes for the dispersed phase would be a better choice.

The effect of particle rotation on characteristics of sphere suspensions was first investigated by Kajishima [68], where it was shown that irrotational spheres develop and maintain clusters, whereas rotational spheres tend to break up clusters frequently as a result of the Magnus lift force and the ensuing horizontal fluctuations. Our observations with cube suspensions appear to be well aligned with the conclusions drawn by Kajishima [68]. We have demonstrated that compared to spheres, cubes on average rotate with considerably higher angular velocities, specifically at lower solid volume fractions and higher Galileo numbers [e.g., Ω_h up to three times higher in cube suspensions versus sphere suspensions for $(\mathrm{Ga}, \phi) = (160, 0.01)$]. Such high rotation rates are accompanied by similarly high values of horizontal particle velocity fluctuations, conceivably resulting from both orientation- and rotation-induced (Magnus) lift forces. The existence of stronger transverse forces promotes the chances of escaping clusters for cubes, which we believe is the underlying reason for the remarkably more homogeneous structure of cube suspensions in comparison with sphere suspensions. Furthermore, we also find that cubes are more effective in transferring momentum from the gravity to the horizontal direction, as shown by the ratio of vertical to horizontal particle velocity fluctuations. The strong transverse motions of cubes not only homogenize the suspension structure but also make particle momentum properties more isotropic compared to sphere suspensions.

It is well established in the literature that microstructure undoubtedly affects the average drag force experienced by particles in a suspension. We confirmed in the present study that the drag on sphere suspensions can be even lower than their fixed-bed counterparts, [e.g., for $(\mathrm{Ga}, \phi) = (160, 0.01)$] due to the shielding effect caused by strong vertical clustering, whereas it can also be higher than fixed beds when particles aggregate horizontally. Except for $(\mathrm{Ga}, \phi) = (160, 0.01)$, however, drag of cube suspensions appears to closely follow that obtained from fixed-bed simulations with the same parameters and random particle distributions. The greater homogeneity of cube suspensions is certainly an important factor responsible for this interesting and rather unexpected behavior. We have depicted in Figs. 14(a) and 14(b) the marked presence of wide horizontal accumulation of spheres especially at $\mathrm{Ga} = 160$, while such regions can be hardly detected in cube suspensions. Nonetheless, one might still anticipate higher drag for dynamic cube suspensions compared to fixed beds of cubes, given the higher velocity fluctuations and that the microstructure is still nonrandom. However, it was recently shown in [21] that velocity fluctuations do not necessarily increase the drag in clustered suspensions. Another factor that needs to be taken into account is the motion freedom of cubes in response to the flow in dynamic cube suspensions. Similar to the findings of Rubinstein *et al.* [85] in Stokes conditions, Tavanashad *et al.* [21] have reported that mobility of spheres always decreases the drag also at high Reynolds numbers. For cubes, mobility might also result in the more frequent occurrence of certain orientations that could cause less resistance to the flow around the cubes. Consequently, since the effect of horizontal clustering and higher velocity variance is to enhance the drag, we suggest that the effect of motion freedom for cubes should have a stronger influence in drag reduction in dynamic cube suspensions compared to sphere suspensions. This matter, along with several others that have not been addressed in the present study, such as, e.g., (1) the competing effect of orientation-induced lift force and rotation-induced Magnus force, (2) the significance of the orientation angle of cubes in suspensions on drag, and whether or not cubes have a distribution of orientation angles that differs from that arising by randomly assigning orientations in a fixed-bed simulation, or (3) the relationship between long periods of high-velocity fluctuations and the suspension microstructure for cubes with $\mathrm{Ga} = 160$ and $\phi = 0.01, 0.05$, need to be considered in future works concerning suspensions of cubes.

ACKNOWLEDGMENTS

We greatly appreciate the financial support of the Natural Sciences and Engineering Research Council of Canada (NSERC) via A.W.'s Discovery Grant RGPIN-2016-06572. This research was enabled by support provided by Compute Canada through A.W.'s 2020 Computing Resources for Research Groups allocation qpf-764-ac.

APPENDIX: TIME-MARCHING ALGORITHM

The numerical time-marching algorithm in our DLM-FD method consists of a four-step classical operator-splitting scheme. For each time t^{n+1}, we solve

(1) A classical L^2-projection scheme for the solution of the Navier-Stokes problem: Find $\mathbf{u}^{n+1/2}$ and p^{n+1} such that

$$\frac{\tilde{\mathbf{u}}^{n+1/2} - \mathbf{u}^n}{\Delta t} - \frac{1}{2\mathrm{Ga}}\nabla^2\tilde{\mathbf{u}}^{n+1/2} = -\boldsymbol{\nabla} p^n + \frac{1}{2\mathrm{Ga}}\nabla^2\mathbf{u}^n - \frac{1}{2}(3\mathbf{u}^n \cdot \boldsymbol{\nabla}\mathbf{u}^n - \mathbf{u}^{n-1} \cdot \boldsymbol{\nabla}\mathbf{u}^{n-1}) - \lambda^n, \tag{A1a}$$

$$\nabla^2\psi^{n+1} = \frac{1}{\Delta t}\boldsymbol{\nabla} \cdot \tilde{\mathbf{u}}^{n+1/2}, \quad \frac{\partial \psi^{n+1}}{\partial n} = 0 \text{ on } \partial\mathbb{D}, \tag{A1b}$$

$$\mathbf{u}^{n+1/2} = \tilde{\mathbf{u}}^{n+1/2} - \Delta t\boldsymbol{\nabla}\psi^{n+1}, \tag{A1c}$$

$$p^{n+1} = p^n + \psi^{n+1} - \frac{\Delta t}{2\mathrm{Ga}}\nabla^2\psi^{n+1}. \tag{A1d}$$

(2) A purely granular problem, predictor step: Find $\mathbf{V}^{n+1/3}$ and $\boldsymbol{\Omega}^{n+1/3}$ such that

$$(m-1)v_p\frac{\mathbf{V}^{n+1/3} - \mathbf{V}^n}{\Delta t} = (m-1)v_p\mathbf{g} + \sum_j \mathbf{F}_{cj}, \tag{A2}$$

$$(m-1)\mathbf{I}_p\frac{\boldsymbol{\Omega}^{n+1/3} - \boldsymbol{\Omega}^n}{\Delta t} = \sum_j \mathbf{r}_j \times \mathbf{F}_{cj} - (m-1)\boldsymbol{\Omega}^n \times \mathbf{I}_p \cdot \boldsymbol{\Omega}^n, \tag{A3}$$

and update particle position $\mathbf{X}^{n+1/3}$.

(3) A fictitious domain problem: Find $\mathbf{u}^{n+1}$, $\mathbf{V}^{n+2/3}$, $\boldsymbol{\Omega}^{n+2/3}$ and λ^{n+1} such that

$$\frac{\mathbf{u}^{n+1} - \mathbf{u}^{n+1/2}}{\Delta t} + \lambda^{n+1} = \lambda^n, \tag{A4}$$

$$(m-1)v_p\frac{\mathbf{V}^{n+2/3} - \mathbf{V}^{n+1/3}}{\Delta t} - \int_{\mathbb{P}} \lambda^{n+1} d\mathbf{x} = \mathbf{0}, \tag{A5}$$

$$(m-1)\mathbf{I}_p\frac{\boldsymbol{\Omega}^{n+2/3} - \boldsymbol{\Omega}^{n+1/3}}{\Delta t} - \int_{\mathbb{P}} \mathbf{r} \times \lambda^{n+1} d\mathbf{x} = \mathbf{0}, \tag{A6}$$

$$\mathbf{u}^{n+1} - (\mathbf{V}^{n+2/3} + \boldsymbol{\Omega}^{n+2/3} \times \mathbf{r}) = \mathbf{0} \text{ in } \mathbb{P}. \tag{A7}$$

(4) A purely granular problem, corrector step: Set $\mathbf{X}^{n+2/3} = \mathbf{X}^{n}$, and find $\mathbf{V}^{n+1}$ and $\boldsymbol{\Omega}^{n+1}$ such that

$$(m-1)v_p \frac{\mathbf{V}^{n+1} - \mathbf{V}^{n+2/3}}{\Delta t} = \sum_j \mathbf{F}_{cj}, \tag{A8}$$

$$(m-1)\mathbf{I}_p \frac{\boldsymbol{\Omega}^{n+1} - \boldsymbol{\Omega}^{n+2/3}}{\Delta t} = \sum_j \mathbf{r}_j \times \mathbf{F}_{cj}, \tag{A9}$$

and update particle position $\mathbf{X}^{n+1}$.

In the above equations, Δt denotes the time step, ψ the pseudopressure and $\partial\mathbb{D}$ the domain boundary. In Eq. (A1a) we use Crank-Nicolson and Adams-Bashforth schemes which are second-order accurate in time to discretize the viscous and advective terms, respectively, while the saddle-point problem in step 3 is handled by an Uzawa algorithm [51]. Considering the high-order correction of the pressure, the projection scheme in step 1 is also second-order accurate in time. However, the first-order time discretization of the fictitious domain sub-problem in step 3, and the overall first-order Marchuk-Yanenko operator-splitting method reduce the global time accuracy of our algorithm to first order only. Equations presented in step 1 are spatially discretized with a second-order central scheme for the diffusion term, whereas the advective term is treated with a total variation diminishing scheme combined with a Superbee flux limiter. Despite the second-order discretization of the flow equations, the accuracy of our method is between first and second order due to the presence of rigid bodies immersed within the computational domain.

---

[1] M. Uhlmann and T. Doychev, Sedimentation of a dilute suspension of rigid spheres at intermediate Galileo numbers: The effect of clustering upon the particle motion, J. Fluid Mech. **752**, 310 (2014).

[2] A. A. Zaidi, T. Tsuji, and T. Tanaka, Direct numerical simulation of finite sized particles settling for high Reynolds number and dilute suspension, Int. J. Heat Fluid Flow **50**, 330 (2014).

[3] G. G. Stokes, On the effect of the internal friction of fluids on the motion of pendulums, Trans. Cambridge Philos. Soc. **9**, 8 (1851).

[4] É Guazzelli, J. F. Morris, and S. Pic, *A Physical Introduction to Suspension Dynamics*, Cambridge Texts in Applied Mathematics (Cambridge University Press, New York, 2011).

[5] G. K. Batchelor, Sedimentation in a dilute dispersion of spheres, J. Fluid Mech. **52**, 245 (1972).

[6] J. F. Richardson and W. N. Zaki, Sedimentation and fluidisation: Part I, Trans. Inst. Chem. Eng. **32**, 35 (1954).

[7] W. Fornari, M. N. Ardekani, and L. Brandt, Clustering and increased settling speed of oblate particles at finite Reynolds number, J. Fluid Mech. **848**, 696 (2018).

[8] W. Fornari, F. Picano, and L. Brandt, Sedimentation of finite-size spheres in quiescent and turbulent environments, J. Fluid Mech. **788**, 640 (2016).

[9] J. Garside and M. R. Al-Dibouni, Velocity-voidage relationships for fluidization and sedimentation in solid-liquid systems, Ind. Eng. Chem. Proc. Design Dev. **16**, 206 (1977).

[10] R. Di Felice, The sedimentation velocity of dilute suspensions of nearly monosized spheres, Int. J. Multiphase Flow **25**, 559 (1999).

[11] X. Yin and D. L. Koch, Hindered settling velocity and microstructure in suspensions of solid spheres with moderate Reynolds numbers, Phys. Fluids **19**, 093302 (2007).

[12] A. Hamid, J. J. Molina, and R. Yamamoto, Direct numerical simulations of sedimenting spherical particles at non-zero Reynolds number, RSC Adv. **4**, 53681 (2014).

[13] R. L. Panton, Flow at low Reynolds numbers, in *Incompressible Flow* (John Wiley & Sons, Hoboken, New Jersey, 2013).

[14] D. L. Koch, Hydrodynamic diffusion in dilute sedimenting suspensions at moderate Reynolds numbers, Phys. Fluids A **5**, 1141 (1993).

[15] A. F. Fortes, D. D. Joseph, and T. S. Lundgren, Nonlinear mechanics of fluidization of beds of spherical particles, J. Fluid Mech. **177**, 467 (1987).

[16] D. P. Willen and A. Prosperetti, Resolved simulations of sedimenting suspensions of spheres, Phys. Rev. Fluids **4**, 014304 (2019).

[17] W. Fornari, S. Zade, L. Brandt, and F. Picano, Settling of finite-size particles in turbulence at different volume fractions, Acta Mech. **230**, 413 (2018).

[18] S. G. Huisman, T. Barois, M. Bourgoin, A. Chouippe, T. Doychev, P. Huck, C. E. B. Morales, M. Uhlmann, and R. Volk, Columnar structure formation of a dilute suspension of settling spherical particles in a quiescent fluid, Phys. Rev. Fluids **1**, 074204 (2016).

[19] E. Climent and M. R. Maxey, Numerical simulations of random suspensions at finite Reynolds numbers, Int. J. Multiphase Flow **29**, 579 (2003).

[20] T. Kajishima and S. Takiguchi, Interaction between particle clusters and particle-induced turbulence, Int. J. Heat Fluid Flow **23**, 639 (2002).

[21] V. Tavanashad, A. Passalacqua, and S. Subramaniam, Particle-resolved simulation of freely evolving particle suspensions: Flow physics and modeling, Int. J. Multiphase Flow **135**, 103533 (2021).

[22] A. Seyed-Ahmadi and A. Wachs, Microstructure-informed probability-driven point-particle model for hydrodynamic forces and torques in particle-laden flows, J. Fluid Mech. **900**, A21 (2020).

[23] R. Natarajan and A. Acrivos, The instability of the steady flow past spheres and disks, J. Fluid Mech. **254**, 323 (1993).

[24] R. H. Magarvey and R. L. Bishop, Transition ranges for three-dimensional wakes, Can. J. Phys. **39**, 1418 (1961).

[25] M. Horowitz and C. H. K. Williamson, The effect of Reynolds number on the dynamics and wakes of freely rising and falling spheres, J. Fluid Mech. **651**, 251 (2010).

[26] M. Jenny, J. Dušek, and G. Bouchet, Instabilities and transition of a sphere falling or ascending freely in a Newtonian fluid, J. Fluid Mech. **508**, 201 (2004).

[27] W. Zhou and J. Dušek, Chaotic states and order in the chaos of the paths of freely falling and ascending spheres, Int. J. Multiphase Flow **75**, 205 (2015).

[28] M. Rahmani and A. Wachs, Free falling and rising of spherical and angular particles, Phys. Fluids **26**, 083301 (2014).

[29] P. Ern, F. Risso, D. Fabre, and J. Magnaudet, Wake-induced oscillatory paths of bodies freely rising or falling in fluids, Annu. Rev. Fluid Mech. **44**, 97 (2012).

[30] J.-L. Pierson, F. Auguste, A. Hammouti, and A. Wachs, Inertial flow past a finite-length axisymmetric cylinder of aspect ratio 3: Effect of the yaw angle, Phys. Rev. Fluids **4**, 044802 (2019).

[31] S. K. P. Sanjeevi, J. A. M. Kuipers, and J. T. Padding, Drag, lift and torque correlations for non-spherical particles from Stokes limit to high Reynolds numbers, Int. J. Multiphase Flow **106**, 325 (2018).

[32] A. Hölzer and M. Sommerfeld, Lattice Boltzmann simulations to determine drag, lift and torque acting on non-spherical particles, Comput. Fluids **38**, 572 (2009).

[33] F. Auguste and J. Magnaudet, Path oscillations and enhanced drag of light rising spheres, J. Fluid Mech. **841**, 228 (2018).

[34] M. Chrust, G. Bouchet, and J. Dušek, Numerical simulation of the dynamics of freely falling discs, Phys. Fluids **25**, 044102 (2013).

[35] H. Zhong, S. Chen, and C. Lee, Experimental study of freely falling thin disks: Transition from planar zigzag to spiral, Phys. Fluids **23**, 011702 (2011).

[36] F. Auguste, J. Magnaudet, and D. Fabre, Falling styles of disks, J. Fluid Mech. **719**, 388 (2013).

[37] P. C. Fernandes, P. Ern, F. Risso, and J. Magnaudet, On the zigzag dynamics of freely moving axisymmetric bodies, Phys. Fluids **17**, 098107 (2005).

[38] V. Mathai, X. Zhu, C. Sun, and D. Lohse, Mass and Moment of Inertia Govern the Transition in the Dynamics and Wakes of Freely Rising and Falling Cylinders, Phys. Rev. Lett. **119**, 054501 (2017).

[39] M. Horowitz and C. H. K. Williamson, Vortex-induced vibration of a rising and falling cylinder, J. Fluid Mech. **662**, 352 (2010).

[40] M. N. Ardekani, P. Costa, W. P. Breugem, and L. Brandt, Numerical study of the sedimentation of spheroidal particles, Int. J. Multiphase Flow **87**, 16 (2016).

[41] A. Seyed-Ahmadi and A. Wachs, Dynamics and wakes of freely settling and rising cubes, Phys. Rev. Fluids **4**, 074304 (2019).

[42] O. Shardt and J. J. Derksen, Direct simulations of dense suspensions of non-spherical particles, Int. J. Multiphase Flow **47**, 25 (2012).

[43] J. J. Derksen, Liquid fluidization with cylindrical particles: Highly resolved simulations, AIChE J. **65**, e16594 (2019).

[44] A. Hamid, A. B. Arshad, S. Mehdi, M. D. Qasim, A. Ullah, J. J. Molina, and R. Yamamoto, A numerical study of sedimentation of rod like particles using smooth profile method, Int. J. Multiphase Flow **127**, 103263 (2020).

[45] B. Herzhaft and É. Guazzelli, Experimental study of the sedimentation of dilute and semi-dilute suspensions of fibres, J. Fluid Mech. **384**, 133 (1999).

[46] A. A. Banaei, M. Rahmani, D. M. Martinez, and L. Brandt, Inertial settling of flexible fiber suspensions, Phys. Rev. Fluids **5**, 024301 (2020).

[47] G. Z. Chen and D. J. Fray, A morphological study of the FFC chromium and titanium powders, Proc. Extract. Metal. **115**, 49 (2006).

[48] F. Y. Fraige, P. A. Langston, and G. Z. Chen, Distinct element modeling of cubic particle packing and flow, Powder Technol. **186**, 224 (2008).

[49] M. Uhlmann and J. Dušek, The motion of a single heavy sphere in ambient fluid: A benchmark for interface-resolved particulate flow simulations with significant relative velocities, Int. J. Multiphase Flow **59**, 221 (2014).

[50] R. Glowinski, T. W. Pan, T. I. Hesla, and D. D. Joseph, A distributed Lagrange multiplier/fictitious domain method for particulate flows, Int. J. Multiphase Flow **25**, 755 (1999).

[51] A. Wachs, A. Hammouti, G. Vinay, and M. Rahmani, Accuracy of finite volume/staggered grid distributed lagrange multiplier/fictitious domain simulations of particulate flows, Comput. Fluids **115**, 154 (2015).

[52] A. Wachs, L. Girolami, G. Vinay, and G. Ferrer, Grains3D, a flexible DEM approach for particles of arbitrary convex shape—Part I: Numerical model and validations, Powder Technol. **224**, 374 (2012).

[53] A. Wachs, PeliGRIFF, a parallel DEM-DLM/FD direct numerical simulation tool for 3D particulate flows, J. Eng. Math. **71**, 131 (2010).

[54] A. Wachs, A DEM-DLM/FD method for direct numerical simulation of particulate flows: Sedimentation of polygonal isometric particles in a Newtonian fluid with collisions, Comput. Fluids **38**, 1608 (2009).

[55] A. Dviugys and B. Peters, An approach to simulate the motion of spherical and non-spherical fuel particles in combustion chambers, Granular Matter **3**, 231 (2001).

[56] M. Jenny, G. Bouchet, and J. Dušek, Nonvertical ascension or fall of a free sphere in a Newtonian fluid, Phys. Fluids **15**, L9 (2003).

[57] É. Guazzelli and J. Hinch, Fluctuations and instability in sedimentation, Annu. Rev. Fluid Mech. **43**, 97 (2011).

[58] X. Yin and D. L. Koch, Velocity fluctuations and hydrodynamic diffusion in finite-Reynolds-number sedimenting suspensions, Phys. Fluids **20**, 043305 (2008).

[59] A. A. Zaidi, T. Tsuji, and T. Tanaka, Hindered settling velocity & structure formation during particle settling by direct numerical simulation, Procedia Eng. **102**, 1656 (2015).

[60] H. Nicolai, B. Herzhaft, E. J. Hinch, L. Oger, and E. Guazzelli, Particle velocity fluctuations and hydrodynamic self-diffusion of sedimenting non-Brownian spheres, Phys. Fluids **7**, 12 (1995).

[61] A. A. Zaidi, Particle velocity distributions and velocity fluctuations of non-Brownian settling particles by particle-resolved direct numerical simulation, Phys. Rev. E **98**, 053103 (2018).

[62] R. J. Freund, D. Mohr, and W. J. Wilson, *Statistical Methods* (Elsevier, 2010).

[63] A. Richter and P. A. Nikrityuk, New correlations for heat and fluid flow past ellipsoidal and cubic particles at different angles of attack, Powder Technol. **249**, 463 (2013).

[64] A. Esteghamatian, M. Bernard, M. Lance, A. Hammouti, and A. Wachs, Micro/meso simulation of a fluidized bed in a homogeneous bubbling regime, Int. J. Multiphase Flow **92**, 93 (2017).

[65] P. M. Kulkarni and J. F. Morris, Suspension properties at finite Reynolds number from simulated shear flow, Phys. Fluids **20**, 040602 (2008).

[66] J. K. Percus and G. J. Yevick, Analysis of classical statistical mechanics by means of collective coordinates, Phys. Rev. **110**, 1 (1958).

[67] R. Kurose and S. Komori, Drag and lift forces on a rotating sphere in a linear shear flow, J. Fluid Mech. **384**, 183 (1999).

[68] T. Kajishima, Influence of particle rotation on the interaction between particle clusters and particle-induced turbulence, Int. J. Heat Fluid Flow **25**, 721 (2004).

[69] C. Y. Wen and Y. H. Yu, Mechanics of fluidization, Chem. Eng. Prog. Symp. Ser. **62**, 100 (1966).

[70] J. M. Dallavalle, *Micromeritics: The Technology of Fine Particles*, 2nd ed. (Pitman Publishing, New York, 1948).

[71] L. Schiller and A. Naumann, Über die grundlegenden Berechnungen bei der Schwerkraftaufbereitung, Z. Ver. Dtsch. Ing. **77**, 318 (1933).

[72] D. Gidaspow, *Multiphase Flow and Fluidization: Continuum and Kinetic Theory Descriptions* (Elsevier Science, 1994).

[73] R. Di Felice, The voidage function for fluid-particle interaction systems, Int. J. Multiphase Flow **20**, 153 (1994).

[74] S. Ergun, Fluid flow through packed columns, Chem. Eng. Prog. **48**, 89 (1952).

[75] R. J. Hill, D. L. Koch, and A. J. C. Ladd, Moderate-Reynolds-number flows in ordered and random arrays of spheres, J. Fluid Mech. **448**, 243 (2001).

[76] R. J. Hill, D. L. Koch, and A. J. C. Ladd, The first effects of fluid inertia on flows in ordered and random arrays of spheres, J. Fluid Mech. **448**, 213 (2001).

[77] R. Beetstra, M. A. van der Hoef, and J. A. M. Kuipers, Drag force of intermediate Reynolds number flow past mono- and bidisperse arrays of spheres, AIChE J. **53**, 489 (2007).

[78] Y. Tang, E. A. Peters, J. A. Kuipers, S. H. Kriebitzsch, and M. A. van der Hoef, A new drag correlation from fully resolved simulations of flow past monodisperse static arrays of spheres, AIChE J. **61**, 688 (2015).

[79] S. Bogner, S. Mohanty, and U. Rüde, Drag correlation for dilute and moderately dense fluid-particle systems using the lattice Boltzmann method, Int. J. Multiphase Flow **68**, 71 (2015).

[80] S. Tenneti, R. Garg, and S. Subramaniam, Drag law for monodisperse gas–solid systems using particle-resolved direct numerical simulation of flow past fixed assemblies of spheres, Int. J. Multiphase Flow **37**, 1072 (2011).

[81] Y. Chen and C. R. Müller, Development of a drag force correlation for assemblies of cubic particles: The effect of solid volume fraction and Reynolds number, Chem. Eng. Sci. **192**, 1157 (2018).

[82] R. Di Felice, Hydrodynamics of liquid fluidisation, Chem. Eng. Sci. **50**, 1213 (1995).

[83] Y. Tang, E. A. J. F. Peters, and J. A. M. Kuipers, Direct numerical simulations of dynamic gas-solid suspensions, AIChE J. **62**, 1958 (2016).

[84] A. A. Zaidi, Particle resolved direct numerical simulation of free settling particles for the study of effects of momentum response time on drag force, Powder Technol. **335**, 222 (2018).

[85] G. J. Rubinstein, J. J. Derksen, and S. Sundaresan, Lattice Boltzmann simulations of low-Reynolds-number flow past fluidized spheres: Effect of Stokes number on drag force, J. Fluid Mech. **788**, 576 (2016).